2D Materials

PAPER

RECEIVED
22 March 2023

REVISED
7 June 2023

ACCEPTED FOR PUBLICATION
12 June 2023

PUBLISHED
29 June 2023

Network of chiral one-dimensional channels and localized states emerging in a moiré system

Jeyong Park[1], Lasse Gresista[1], Simon Trebst[1], Achim Rosch[1] and Jinhong Park[1,2,*]

[1] Institute for Theoretical Physics, University of Cologne, 50937 Cologne, Germany
[2] Institute for Quantum Materials and Technologies, Karlsruhe Institute of Technology, 76021 Karlsruhe, Germany
* Author to whom any correspondence should be addressed.

E-mail: jinhong.park@kit.edu

Keywords: moiré system, network of chiral 1D channels and localized states, chiral order, quantum and classical fluctuations

Abstract

Moiré systems provide a highly tunable platform for engineering band structures and exotic correlated phases. Here, we theoretically study a model for a single layer of graphene subject to a smooth moiré electrostatic potential, induced by an insulating substrate layer. For sufficiently large moiré unit cells, we find that ultra-flat bands coexist with a triangular network of chiral one-dimensional (1D) channels. These channels mediate an effective interaction between localized modes with spin-, orbital- and valley degrees of freedom emerging from the flat bands. The form of the interaction reflects the chirality and 1D nature of the network. We study this interacting model within an $SU(4)$ mean-field theory, semi-classical Monte-Carlo simulations, and an $SU(4)$ spin-wave theory, focusing on commensurate order stabilized by local two-site and chiral three-site interactions. By tuning a gate voltage, one can trigger a non-coplanar phase characterized by a peculiar coexistence of three different types of order: ferromagnetic spin order in one valley, non-coplanar chiral spin order in the other valley, and 120° order in the remaining spin and valley-mixed degrees of freedom. Quantum and classical fluctuations have qualitatively different effects on the observed phases and can, for example, create a finite spin-chirality purely via fluctuation effects.

1. Introduction

Stacking a two-dimensional van der Waals material on top of other van der Waals materials (with or without a relative twist) defines a class of quantum material known as moiré materials [1, 2]. Due to their highly tunable experimental knobs for engineering band structures, thereby facilitating the emergence of correlated phases [3–7], such moiré materials have recently met with tremendous interest. A prototypical example is twisted bilayer graphene (TBG) [8–10], where two sheets of graphene are stacked with a relative twist. At twist angles $\sim 1.1°$, the so-called 'magic angle', flat bands emerge near the charge neutrality point [8–11], which amplifies the effect of interaction to exhibit various correlated phases [12–28]. Besides TBG, a wealth of different types of exotic bands and interaction effects have been discovered in multilayer moiré systems [1, 2, 29–35].

In this manuscript, we address one of the simplest models of a moiré system: a *single* layer of graphene subject to a moiré potential induced by a substrate layer. Despite its simplicity, it shows—even without fine tuning—remarkably rich physics. For sufficiently large moiré unit cells two kinds of moiré bands emerge: one-dimensional chiral channels (1DCCs) and ultra-flat bands. Along lines where the gap arising from the moiré potential changes sign, a network of topologically protected 1DCCs is developed, as depicted in figure 1. At the same time, an extra set of localized modes emerges at the junction where six 1DCCs join (red dots in figure 1). These modes only hybridize weakly with the 1DCCs and with the neighboring localized modes giving rise to ultra-flat bands. This coexistence of localized modes and propagating 1DCCs and the resulting peculiar interaction physics are the main results of this paper.

The emergence of a network of 1D chiral channels in moiré systems has been previously discussed

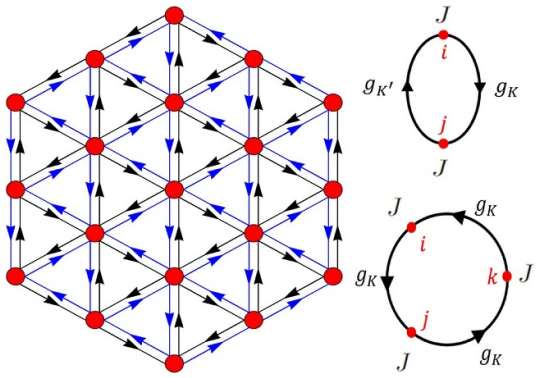

Figure 1. Network model consisting of one-dimensional chiral channels (blue arrows for the K valley, black for the K' valley) and localized states (red circles). Upper (Lower) right: the diagram for the two (three)-spin interaction.

[36–46]. In an early study, San-Jose and Prada [36] pointed out that a network of topologically protected 1D helical channels forms in TBG subject to an out-of-plane electric field, see also [37, 45]. Experimentally, signatures of these 1D channels have been observed in transport [39, 41, 42] and scanning tunneling spectroscopy [40]. In contrast to our model, such systems do not exhibit the coexistence of flat bands and 1D channels. Moreover, a coexistence of propagating *two-dimensional* Dirac dispersing bands and flat bands has been reported in mirror symmetric twisted trilayer graphene [30, 31]. In this setting, Ramires and Lado discussed heavy fermion physics, emerging from the interaction of localized and propagating modes [34]. From a more general point of view, the emergence of localized and propagating bands in moiré systems has been investigated in [47] using concepts of quantum chaos. Generic bands tend *not* to be flat due to localization in *momentum space*, but these arguments cannot be applied to the bands discussed in our paper arising from the specific real-space structure of the moiré potential.

2. Model

We consider a single layer of graphene on top of some *insulating* substrate which shares the hexagonal structure with graphene but has either a slightly different lattice constant or is rotated by a small twist angle. As the substrate is gapped, it mainly affects graphene via electrostatic potential terms. Thus, at low-energies, the spinless single-particle Hamiltonian is approximated by

$$H_{\text{eff}} = -iv(\partial_x s^x \tau^z + \partial_y s^y \tau^0) + V_0(\boldsymbol{r})\mathbb{1} + V_s(\boldsymbol{r}) s^z. \tag{1}$$

Here the Pauli matrices τ^i and s^i act on the valley and sublattice space, respectively, and v is the graphene Fermi velocity. The staggered term $V_s = (V_A - V_B)/2$ describes the potential difference between the A and B sublattice, V_A and V_B, and a constant V_s opens a mass gap in the Dirac spectrum. The magnitude of V_s has a maximum in regions of the moiré lattice where the atoms of different sublattices stack on the top of each other, i.e. AB or BA stacking as shown in figure 2(a). The uniform potential V_0 is given by $V_0 = (V_A + V_B)/2$. Due to the smoothness of moiré structures, we can focus on the lowest Fourier components of the potentials. Denoting the six smallest reciprocal lattice vectors of the moiré structure by $\boldsymbol{G}_i$, $i = 1, \ldots, 6$, with $|\boldsymbol{G}_i| \equiv G = \frac{4\pi}{\sqrt{3}L}$, we obtain

$$V_\beta(\boldsymbol{r}) = \sum_{\beta'=A,B} \sum_{i=1}^{6} u_{\beta\beta'} e^{i\boldsymbol{G}_i \cdot (\boldsymbol{r} - \boldsymbol{r}_{\beta\beta'})} \tag{2}$$

with sublattice $\beta = A, B$, the size of moiré unit cell L, and $\boldsymbol{r}_{AA} = \boldsymbol{r}_{BB} = 0$, $\boldsymbol{r}_{AB} = -\boldsymbol{r}_{BA}$, see figure 2(a). Here, we neglect the effect of a possible quasi-periodic structure of the moiré potentials assuming L is sufficiently larger than the atomic distance [10]. We consider a hexagonal substrate with equivalent A and B sublattices such that $u_{AA} = u_{BB}$ and $u_{AB} = u_{BA}$. In this case, the amplitudes of V_s and V_0 are given by $u_s = u_{AB}$ and $u_0 = -2u_{AA} + u_{AB}$. The Hamiltonian (equations (1) and (2)) relies on the presence of an insulating 2D or 3D substrate with a honeycomb (surface) structure and a lattice constant similar to graphene. In appendix C we discuss that the same type of physics can also approximately be realized for different types of substrates with lower symmetry like hexagonal boron nitrite (h-BN) as long as moiré corrugation effects do not become too large. As a concrete model, we investigate in appendix C a twisted monolayer bilayer graphene (TMBG), which has recently been realized experimentally [48], and show that this material is an excellent candidate for an approximate realization of our model.

As shown in figure 2(b), V_s vanishes along straight lines and thus changes its sign across those lines. At the same time, V_0 has minima at high-symmetry points (red dots) in the center of the moiré unit cell where the lines cross. These two regions lead to two very different types of bands: 1D dispersing bands and ultra-flat bands, see figure 2(c), computed by diagonalizing equation (1) in momentum space.

2.1. 1DCCs

The sign change of the mass term $V_s(\boldsymbol{r})$ induces a 1DCC, propagating along the straight lines in figure 2(b) with the full speed of the graphene Fermi velocity. 1DCCs emerging from the K and K' valley move in opposite directions, as depicted by black and blue arrows in figures 1 and 2(f) shows the Bloch wave function of the propagating bands which perfectly tracks the straight lines in figure 2(b). Surprisingly, the wave functions show almost no modulation at their crossing points.

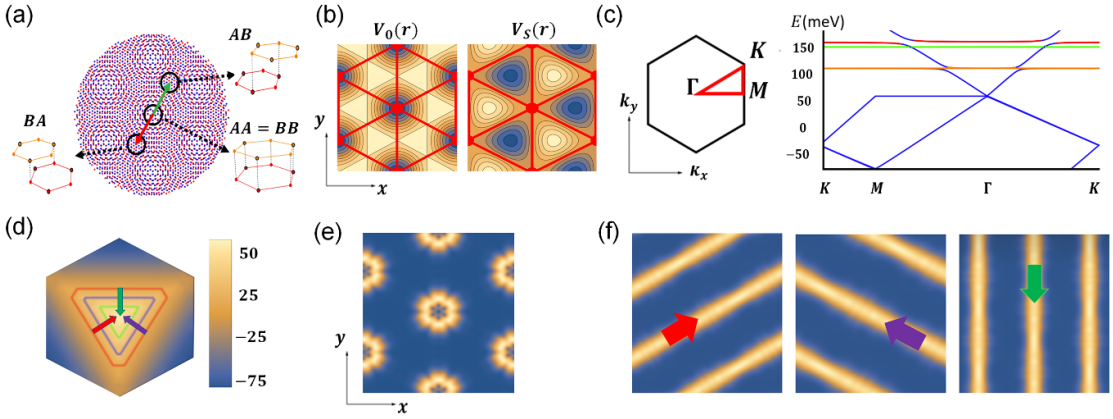

Figure 2. Moiré potential model. (a) Moiré pattern from a layer of the hexagonal lattice (blue dots) stacked on top of another layer of an hexagonal lattice (red). Due to a relative rotation of the layers, different local stacking patterns (AA, AB, BA) occur (circles). The vectors $\boldsymbol{r}_{AB} = -\boldsymbol{r}_{BA} = (\frac{\sqrt{3}L}{6}, \frac{L}{2})$ connect regions of AA and AB stacking. (b) The uniform and staggered potential, $V_0(\boldsymbol{r})$ and $V_s(\boldsymbol{r})$, in real space. (c) Band structure for the effective Hamiltonian equation (1) in the moiré Brillouin zone. Flat bands are classified by different representations (red: ρ_3, green: ρ_4, orange: ρ_6) of the symmetry group Dic_3. (d) Density plot of the energy for one of the one-dimensional (1D) dispersing bands and the Fermi surfaces at three different chemical potentials (red 0 meV, blue 20 meV, green 40 meV). The arrows indicate the three different propagating directions. (e) Bloch wave functions $|\Psi_{n,\boldsymbol{k}}(\boldsymbol{r})|^2$ of the green flat band at the Γ point. (f) Bloch wave functions of 1D propagating bands at momenta indicated by the arrows in (d). Parameters: $u_{AA} = u_{BB} = 0$ and $u_{AB} = u_{BA} = \frac{8\pi v}{\sqrt{3}L}$.

The 1DCCs get more stable when u_s is sufficiently strong. Expanding V_s around a $V_s = 0$ line, $V_s \sim 8\pi u_s \Delta x/L$, and employing a scaling analysis for equation (1), one finds that the width of these 1DCCs is given by $d_{1\mathrm{D}} \sim (vL/(8\pi u_s))^{1/2}$. For sufficiently large moiré sizes, $L \gg d_{1\mathrm{D}}$, or equivalently, $L \gg v/(8\pi u_s)$, 1DCCs and localized modes are realized with an exponential suppression of, e.g. the hybridization of neighboring 1D channels. For the parameters of figure 2 these estimates give $d_{1\mathrm{D}} \approx 0.05\,L$ consistent with our numerical results.

2.2. Localized states

The flat bands in figure 2(c) have their origins in states localized close to the red dots in figure 2(b), where V_0 has a minimum whereas V_s is highly suppressed. A sufficiently strong moiré potential (more precisely, $u_0 \gg v/(8\pi^2 L)$, see section 2.1) renders the states localized in real space as shown in figure 2(e). These localized modes hybridize only weakly with the 1DCCs and neighboring localized modes, leading to ultra-flat bands. The localized states with fixed valley index can be classified by the dicyclic symmetry group Dic_3. From Dic_3, one obtains three different types of localized states, labeled by two 1D representations ρ_3, ρ_4 and a two-dimensional irreducible representation ρ_6, see appendix A.

2.3. Network model

Combining localized and propagating states, we obtain the network model depicted in figure 1. The kinetic Hamiltonian for the 1DCCs is given by

$$H_{\mathrm{kin}} = -iv \sum_{\alpha,n,i,\sigma} \alpha \int \mathrm{d}\rho \Psi^{\dagger}_{n,i,\alpha,\sigma}(\rho)\partial_\rho \Psi_{n,i,\alpha,\sigma}(\rho). \tag{3}$$

The operator $\Psi^{\dagger}_{n,i,\alpha,\sigma}(\rho)$ creates an electron with spin $\sigma = \uparrow / \downarrow$ and valley $\alpha = \pm = K/K'$ in a 1DCC propagating along the lattice vector $\boldsymbol{a}_i$ with $i = 1, 2, 3$; the center of the corresponding wave packet is located at $\boldsymbol{R}_{n,i,\rho} = n\boldsymbol{a}_{i+1} + \rho \boldsymbol{a}_i$ with integer n. We denote the location of crossing points of 1DCCs by $\boldsymbol{R}_m$ and define $\rho_{n,i,m}$ as the solution of $\boldsymbol{R}_m = \boldsymbol{R}_{n,i,\rho_{n,i,m}}$. In these notations, the inter-channel tunneling H_w and the coupling of 1DCCs to localized states, H_λ, are given by

$$H_w = \sum_{\text{crossing at } \boldsymbol{R}_m} \hat{w}_{ii'} \Psi^{\dagger}_{n,i,\alpha,\sigma}(\rho_{n,i,m}) \Psi_{n',i',\alpha,\sigma}(\rho_{n',i',m}),$$
$$H_\lambda = \sum_{\text{crossing at } \boldsymbol{R}_m} \hat{\lambda}_{ij} d^{\dagger}_{m,\alpha,\sigma,j} \Psi_{n,i,\alpha,\sigma}(\rho_{n,i,m}) + h.c.\,. \tag{4}$$

We sum over all channels which cross at $\boldsymbol{R}_m$. $d^{\dagger}_{m,\alpha,\sigma,j}$ creates localized electronic states where j denotes an extra orbital index if the localized states belong to the ρ_6 representation. The form of the matrices $\hat{w}_{ii'}$ and $\hat{\lambda}_{ij}$ is entirely determined by the symmetries of the system and the representation of Dic_3 of the localized states. Equations (3) and (4) describe the bandstructure with high precision after fitting the amplitude of $\hat{w}$ and $\hat{\lambda}$ and the energy of the localized states, see appendix B.

2.4. Local interaction

Since the flat bands are highly localized, there will be a Coulomb blockade for adding electrons to the localized sites, described by

$$H_U = U \sum_{\boldsymbol{R}_m} \sum_{\xi \neq \xi'} n_{m,\xi} n_{m,\xi'}, \tag{5}$$

where $\xi = \{\alpha, \sigma\}$ includes all local quantum numbers, i.e. valley α and spin σ (and an extra orbital

quantum number for the ρ_6 representation). Since for large moiré unit cells the dominant contribution comes from the long-ranged part of the Coulomb interaction which is only sensitive to charge, H_U is approximately $SU(4)$ (or $SU(8)$ for ρ_6) invariant. Using $U \sim \frac{e^2}{4\pi\epsilon_0 d_{\rm loc}}$ with $d_{\rm loc} \approx 6.3$ nm, we estimate $U \approx 230$ meV for the parameters of figure 2(e) which is more than an order of magnitude larger than the hybridization of impurity levels, λ.

As $U \gg \lambda$, the system maps to a (generalized) Kondo lattice model, where local degrees of freedom couple only via the network of 1DCCs. For a localized state in the ρ_4 representation, one obtains an effective SU(4) symmetric coupling

$$H_J \approx JL \sum_{\text{crossing at } \boldsymbol{R}_m} \Gamma^\ell(\boldsymbol{R}_m)\cdot\tilde{\Psi}^\dagger_\xi(\boldsymbol{R}_m)\gamma^\ell_{\xi\xi'}\tilde{\Psi}_{\xi'}(\boldsymbol{R}_m). \tag{6}$$

Here γ^ℓ, $\ell = 1,\ldots,15$, are the 4×4 generators of $SU(4)$ acting on a linear combination of the three 1DCCs resulting from the hybridization matrix $\hat{\lambda}$ (see appendix A), $\tilde{\Psi}_\xi(\boldsymbol{R}_m) = \frac{1}{\sqrt{3}}\sum_{i=1,2,3}(-1)^i \Psi_{n_i,i,\xi}(\rho_{n_i,i,m})$, and $\Gamma^\ell(\boldsymbol{R}_m) = \sum_{\xi,\xi'} d^\dagger_{m,\xi}\gamma^\ell_{\xi\xi'}d_{m,\xi'}$ describes the local $SU(4)$ degree of freedom. $J \sim \lambda^2/U$ is the Kondo coupling that originates from the hybridization of the 1DCCs with the localized states.

The interaction between the localized states is mediated by the network of 1DCCs. The resulting RKKY interaction is obtained from a perturbation theory both in J and the inter-channel tunneling w. From a standard RKKY diagram (see figure 1) to order J^2w^0, we obtain the two-spin interaction term

$$H_{2s} = -\frac{J^2L^2}{12\pi v}\sum_{(m_1\to m_2)_c}\left(\frac{e^{2i\boldsymbol{k}^i_F\cdot\boldsymbol{\rho}_{m_1m_2}}}{|\boldsymbol{\rho}_{m_1m_2}|}\times(1+\boldsymbol{\sigma}_{m_1}\cdot\boldsymbol{\sigma}_{m_2})\tau^-_{m_1}\tau^+_{m_2}+h.c.\right). \tag{7}$$

$\boldsymbol{\sigma}_m \equiv \boldsymbol{\sigma}(\boldsymbol{R}_m)$ and $\boldsymbol{\tau}_m \equiv \boldsymbol{\tau}(\boldsymbol{R}_m)$ are Pauli matrices acting on spin and valley at $\boldsymbol{R}_m$, and $\tau^\pm \equiv \tau^x \pm i\tau^y$. The summation $(m_1\to m_2)_c$ runs only over localized states connected by the same 1DCC, separated by $\boldsymbol{\rho}_{m_1m_2} \equiv \boldsymbol{R}_{m_2} - \boldsymbol{R}_{m_1}$ parallel to the Fermi velocity of the + valley channels. Importantly, the RKKY term necessarily requires two valley flip processes, $\tau^-_{m_1}\tau^+_{m_2}$: both a valley + and − channel running in opposite directions are needed to form a closed loop connecting two sites, see figure 1. This process breaks the $SU(4)$ symmetry.

Closed loops can also be formed by triangles in figure 1, remarkably, inducing a chiral interaction to order J^3. From the diagram depicted in figure 1, we obtain

$$H_{3s} = \frac{8J^3L^3}{27\sqrt{3}\pi v^2}\sum_{p=\triangleright/\triangleleft,(m_1,m_2,m_3)_p}\frac{\cos(3k_F|\boldsymbol{\rho}_{m_1,m_2}|)}{|\boldsymbol{\rho}_{m_1,m_2}|}\times p\,\boldsymbol{\sigma}_{m_1}\cdot(\boldsymbol{\sigma}_{m_2}\times\boldsymbol{\sigma}_{m_3})\left(\prod_{i=1}^3 P^+_{m_i} - \prod_{i=1}^3 P^-_{m_i}\right). \tag{8}$$

The summation runs over the right- and left-oriented triangles, $p = \triangleright/\triangleleft = \pm1$, in figure 1, where $(m_1,m_2,m_3)_p$ denotes the three sites of each triangle (in anti-clockwise order). k_F is the Fermi momentum of 1DCCs. We defined the projector $P^\pm_m \equiv \frac{(\tau^0_m \pm \tau^z_m)}{2}$ on valley $\pm$ at $\boldsymbol{R}_m$. The chiral spin-interaction, $\boldsymbol{\sigma}_{m_1}\cdot(\boldsymbol{\sigma}_{m_2}\times\boldsymbol{\sigma}_{m_3})$, is induced by the chiral motion of the 1DCCs within each triangle (even in the absence of spin-orbit interaction). The direction of the chiral currents determines the sign of the chiral interaction which changes when moving from $\triangleright$ to $\triangleleft$ or from valley + to −.

There is also a non-chiral contribution from the same diagram and from a similar diagram to order J^2w,

$$H'_{2s} = \frac{J^2L^3}{27\sqrt{3}\pi v^2}\sum_{p=\triangleright/\triangleleft,(m_1,m_2,m_3)_p}\frac{\sin(3k_F|\boldsymbol{\rho}_{m_1,m_2}|)}{|\boldsymbol{\rho}_{m_1,m_2}|}\times(1+\boldsymbol{\sigma}_{m_1}\cdot\boldsymbol{\sigma}_{m_2})\left(J\tau^z_{m_3}(\tau^z_{m_1}+\tau^z_{m_2}) + w(1+\tau^z_{m_1}\tau^z_{m_2})\right) + \text{permutations}. \tag{9}$$

We sum over the 6 permutations for renaming m_1, m_2 and m_3.

3. Mean-field phase diagram

To study the interplay of equations (7)–(9), we consider a simplified Hamiltonian which contains only nearest neighbor interactions, $H_{sv} = H_2 + H_3 + H_{2'}$, with

$$\begin{aligned} H_2 &= J_2\sum_{\langle m_1\to m_2\rangle_c}(1+\boldsymbol{\sigma}_{m_1}\cdot\boldsymbol{\sigma}_{m_2})(e^{i\varphi}\tau^+_{m_1}\tau^-_{m_2}+h.c.)\\ H_3 &= J_3\sum_{p=\triangleright/\triangleleft,(m_1,m_2,m_3)_p} p\left(\prod_{i=1}^3 P^+_{m_i} - \prod_{i=1}^3 P^-_{m_i}\right)\times\boldsymbol{\sigma}_{m_1}\cdot(\boldsymbol{\sigma}_{m_2}\times\boldsymbol{\sigma}_{m_3})\\ H_{2'} &= J'_2\sum_{\langle m_1\to m_2\rangle_c}(1+\boldsymbol{\sigma}_{m_1}\cdot\boldsymbol{\sigma}_{m_2})(1+\tau^z_{m_1}\tau^z_{m_2}). \end{aligned} \tag{10}$$

Here $J_2 > 0$ is the largest coupling constant with $\varphi = 2k_FL + \pi$, while $J'_2 \sim \sin(3k_FL)$ and $J_3 \sim \cos(3k_FL)$. Equation (10) contains only nearest neighbor interactions, neglecting the further long-range tails in equations (7)–(9). While the nearest neighbor interactions dominantly determine the phase diagram in most electron fillings of the 1DCCs, the long-range contributions may stabilize incommensurate spin or valley orders in some incommensurate fillings

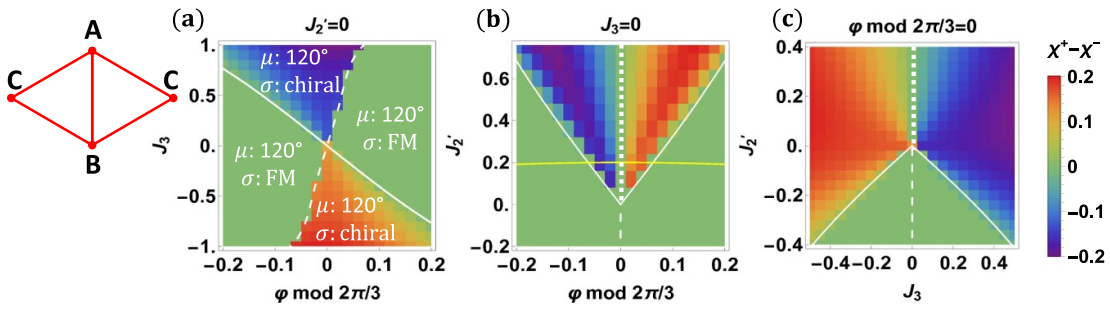

Figure 3. Mean-field phase diagrams with the order parameter, $\chi^+ - \chi^-$, for small J_3, J_2', and φ, defined modulo $2\pi/3$ (cf equation (10)). All phases shown in the figure show a 120° order in the $\boldsymbol{\mu}$ valley degrees of freedom. They differ by their spin order which are distinguished by $\chi^\pm \equiv \langle \boldsymbol{\sigma} P^\pm \rangle_A \cdot \langle \boldsymbol{\sigma} P^\pm \rangle_B \times \langle \boldsymbol{\sigma} P^\pm \rangle_C$, the valley-projected chirality, defined on a triangle (cf the inset). Three different types of spin-order occur: spin-ferromagnetic order (green regions), a chiral spin-order (red or blue regions) in one of the two valleys, and an in-plane 120° spin order in one of the two valleys (white dotted line). J_2 is set to 1. Panel (a): (φ, J_3) space with $J_2' = 0$, panel (b): (φ, J_2') with $J_3 = 0$, panel (**c**): (J_3, J_2') with $\varphi = 0$. The yellow line in panel (b) shows schematically how parameters change as a function of a gate voltage for $k_F L$ close to $-\frac{\pi}{2}$. While the solid white lines represent second order transitions, the dashed white line a first order transition where the type of 120° order changes from left- to right circulating on a triangle ▷ (opening angle $\theta = 0, \pi$, respectively, see appendix D).

of the 1DCCs. But, in this paper, we focus on the effect of the nearest neighbor interactions. From H_{2s}', equation (9), we take, for simplicity, only the term $\sim J^2 w$ into account (assuming $w > J$) but we checked that the J^3 contribution to H_{2s}' does not lead to qualitative changes. The continuous symmetries of $H_{\rm sv}$ are $U(1) \times SU(2) \times SU(2)$ generated by τ^z, $P^+\boldsymbol{\sigma}$ and $P^-\boldsymbol{\sigma}$. Remarkably, one can rotate the spin-orientation of the two valleys independently.

Assuming that the localized states are filled with one electron, the states on the $SU(4)$ space are spanned by a 4-component complex vector. In this basis, we solve the self-consistent mean-field equations at $T = 0$ iteratively. We find that either a one- or a three-sublattice solution has the lowest energy. As J_2 is the largest term, we first analyze the case $J_3 = J_2' = 0$. The parameter φ in equation (10) can be viewed as an Aharonov–Bohm phase arising from a staggered magnetic flux. As 3φ is the total phase along a triangular loop, one can always 'gauge away' changes of φ by $\frac{2\pi}{3}$ using τ_z rotations by 0, $2\pi/3$, $4\pi/3$ on the A, B, C sublattices. For $\varphi = 0$, we obtain a variant of the Kugel–Khomskii model [49]

$$H_0 = 2J_2 \sum_{\langle m_1 \to m_2 \rangle_c} (1 + \boldsymbol{\sigma}_{m_1} \cdot \boldsymbol{\sigma}_{m_2})(\tau^x_{m_1}\tau^x_{m_2} + \tau^y_{m_1}\tau^y_{m_2}) = 2J_2 \sum_{\langle m_1 \to m_2 \rangle_c} \boldsymbol{\mu}^1_{m_1} \cdot \boldsymbol{\mu}^1_{m_2} + \boldsymbol{\mu}^2_{m_1} \cdot \boldsymbol{\mu}^2_{m_2} \qquad (11)$$

with four component vectors given by $\boldsymbol{\mu}^1_m = (\tau^x_m, \tau^y_m\sigma^x_m, \tau^y_m\sigma^y_m, \tau^y_m\sigma^z_m)$ and $\boldsymbol{\mu}^2_m = (\tau^y_m, \tau^x_m\sigma^x_m, \tau^x_m\sigma^y_m, \tau^x_m\sigma^z_m)$. The ground states have a three-site unit-cell where the vectors $\langle \boldsymbol{\mu}^n_m \rangle$, $n = 1, 2$, have the norm 1, and show 120° order such that $\langle \boldsymbol{\mu}^n_{m_1} \rangle \cdot \langle \boldsymbol{\mu}^n_{m_2} \rangle = \cos(2\pi/3) = -\frac{1}{2}$ for neighboring sites. Note that this specific type of 120° order is realized with 4-component vectors. Surprisingly, the above described 120° order has an extra degree of freedom that is revealed by the magnetization vectors $\langle P^\pm \boldsymbol{\sigma} \rangle$ in the two valleys. These vectors have length 1/2 in the ground-state manifold. In one of the two valleys, the magnetization is always ferromagnetic, but in the other valley a non-coplanar spin configuration is possible, leading to a finite staggered chirality $\chi^\pm$ with $\chi^\pm = \langle \boldsymbol{\sigma}_{m_1} P^\pm_{m_1} \cdot (\boldsymbol{\sigma}_{m_2} P^\pm_{m_2} \times \boldsymbol{\sigma}_{m_3} P^\pm_{m_3}) \rangle$. In appendix D, we describe how the mean-field solution can be parameterized by a continuous angle θ and a discrete variable $\pm$, describing the opening angle of non-coplanar valley-projected spins on the three sublattices and also which of the valley sector exhibits ferromagnetic order.

States with an arbitrary chirality, $-\frac{1}{8} \leqslant \chi^\pm \leqslant \frac{1}{8}$, are degenerate (within mean-field theory) if only H_0, equation (11), is considered, see appendix D. Thus, H_0 defines a highly singular point in the phase diagram and even small perturbations can select one of the states in the ground-state manifold of H_0. For example, for an infinitesimal $J_3 > 0$ perturbation, states are selected which have either the minimal value $\chi^+ = -\frac{1}{8}$ with $\chi^- = 0$ or the maximal value of $\chi^- = \frac{1}{8}$ with $\chi^+ = 0$. Such a staggered (or uniform) chiral order has, e.g. been extensively studied in the spin-1/2 [50, 51] or the half-filled Hubbard model [52–55] on the triangular lattice.

In contrast, the perturbation by a finite φ stabilizes a phase where $\langle P^\pm \sigma \rangle$ orders ferromagnetically for both valleys, $\chi^+ = \chi^- = 0$, while $\langle \boldsymbol{\mu}^n \rangle$ displays a coplanar 120° ordered phase. The presence of both φ and J_3 leads to the phase diagram of figure 3(a). A finite $J_2' > 0$, however, suppresses such ferromagnetic configuration, selecting a state where $\langle P^\pm \sigma \rangle$ is non-collinear but coplanar, forming a 120° order in either $\langle P^+ \sigma \rangle$ or $\langle P^- \sigma \rangle$ on top of the 120° order in $\langle \boldsymbol{\mu}^n \rangle$. The resulting phase diagrams are shown in figures 3(b) and (c).

4. Classical fluctuations

The mean-field theory discussed above, ignores the effect of both quantum and classical fluctuations. To capture fluctuation effects, we have (i) performed an $SU(4)$ spin-wave calculation (or, more precisely, spin-valley-wave calculation) both in the classical and quantum regime. Details of the $SU(4)$ spin-wave theory are given in the appendix E. Furthermore, we have (ii) calculated finite temperature properties of the semi-classical version of our $SU(4)$ model using Monte Carlo calculations.

A semi-classical variant of our $SU(4)$ model can formally be obtained by making a product ansatz for the wavefunction, $|\Psi\rangle = \prod_m |\Psi_m\rangle$, where $|\Psi_m\rangle$ is a single-site 4-component normalized wave function with an arbitrary phase per site. A semi-classical state for a system of size $N \times N$ is thus parameterized by $(4 \cdot 2 - 2)N^2$ real numbers. At $T = 0$, this semi-classical model reproduces the mean-field results discussed in section 3. Thermal expectation values at a finite temperature $T = 1/\beta$ can be approximately calculated by sampling the space of product-state wavefunctions according to the Boltzmann distribution $\sim \exp(-\beta\langle\psi|H|\psi\rangle)$ [56, 57] using a standard Markov chain Monte Carlo algorithm [58]. Employing local Metropolis updates, a typical Monte Carlo run consists of $N_m = 1 \cdot 10^6$ thermalization sweeps followed by $N_m = 4 \cdot 10^6$ measurement sweeps, or up to $N_m = 10^7$ sweeps close to the transition temperature. We use linear lattice sizes of up to $N = 72$ with periodic boundary conditions. Additional details on the simulations are provided in appendix F.

As the mean-field ground state of the J_2-only model H_0, equation (11), is degenerate, we focus our discussions on fluctuation effects around this state. The specific heat of the semi-classical model, figure 4(a), shows a sharp peak indicating a finite-temperature phase transition. The numerical data is both consistent with a weak first-order and a second-order transition, see appendix F which also discusses energy distributions at criticality. We analyze two types of order parameters, the spin-chirality, figure 4(b), and the valley-projected ferromagnetic order, figure 4(c), which show very different finite-size and temperature behavior as discussed below.

For $T \to 0$, the spin-chirality, figure 4(b), vanishes while the ferromagnetic magnetization in both valley sectors takes the value $1/2$, figure 4(c). This shows that thermal fluctuations select the spin-ferromagnetic states, $\theta = 0, \pi$ from the ground-state manifold. At the same time, the valley, more precisely $\boldsymbol{\mu}^{1,2}$, exhibits 120° order (not shown). This 'order-by-disorder' selection [60] of the classical ground state in the limit $T \to 0$ is also found within our $SU(4)$ spin wave calculation, see figure 6(b) below and appendix E: a fluctuation correction to the free energy linear in T selects the ferromagnetic state.

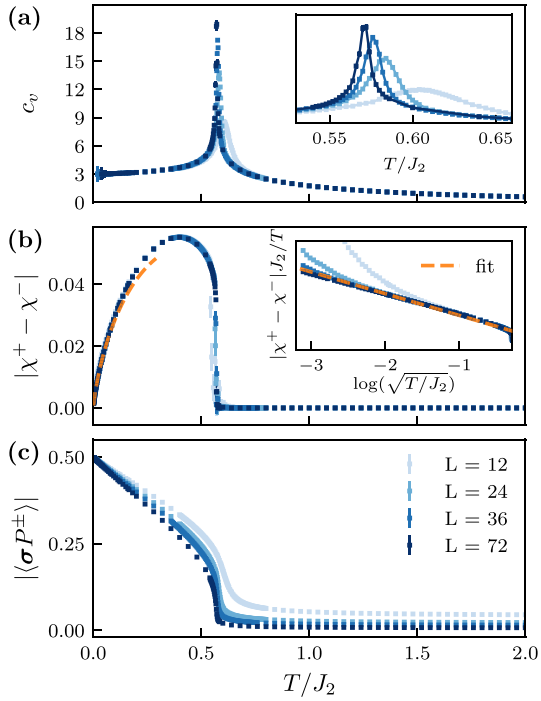

Figure 4. Thermodynamics and thermal order-by-disorder transition. Shown are Monte Carlo results for the J_2 model, equation (11), in the semi-classical approximation for different linear system sizes $N = 12, 24, 36$ and 72. Numerical errors are smaller than the size of the symbols. Panel (a): The specific heat shows a pronounced peak indicating a thermal phase transition which gets sharper upon increasing N. Panel (b): At finite temperature T and inside the ordered phase a finite spin-chirality develops. The T-dependence at low temperature is singular and approximately proportional to $T \log 1/\sqrt{T}$, see inset. Inset: Fit to the analytical result (12) at low T (dashed orange line). Panel (c): By an order-by-disorder mechanism, the system selects a state with ferromagnetic spin order at low T. At finite T the order parameter is suppressed by thermal fluctuations linear in T. The prefactor of the linear correction increases with system size, reflecting the suppression of long-ranged order by thermal fluctuations, consistent with the Mermin–Wagner theorem [59].

At finite T, the ferromagnetic order parameter shown in figure 4(c) is suppressed linearly in T. The prefactor of this suppression increases with system size N. This is explained by an order-parameter suppression $\propto T \ln N$, well known from the Mermin–Wagner theorem [59] in two spatial dimensions. Thus, there is nominally no long-ranged spin-order in the thermodynamic limit.

A remarkable result is that in the spin-ferromagnetic state the spin-chirality becomes finite at finite T, figure 4(b), showing a highly singular T dependence which is almost independent on system size N. In appendix E, we use an $SU(4)$ spin-wave calculation to compute $\langle \hat{\chi}^+ - \hat{\chi}^- \rangle$. The $SU(4)$ spin wave theory is formally derived using a $1/M$ expansion, where M are the number of local bosons, $\sum_{\xi=1}^{4} b^\dagger_{m,\xi} b_{m,\xi} = M$, used to describe the local $SU(4)$ degree of freedom, see appendix E. For $M \to \infty$ one recovers mean-field and spin-waves are computed to

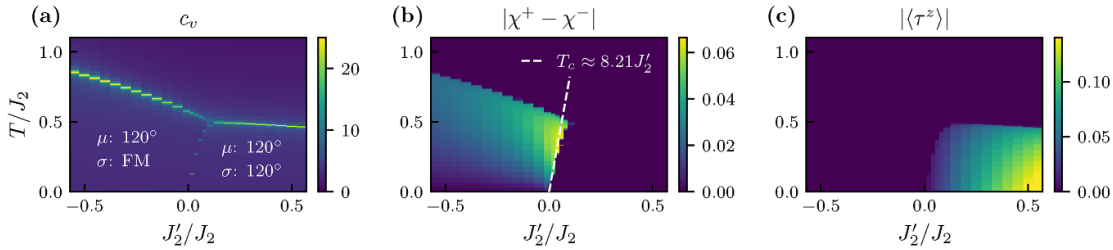

Figure 5. Phase diagram from semi-classical Monte Carlo calculations. Shown is Monte Carlo data for the specific heat (a), spin-chirality (b), and valley-magnetization (c), obtained from simulations of a model with $\varphi = J_3 = 0$ as function of temperature and J_2' for a fixed linear system size $N = 36$. Panel (a): Specific heat. At high temperatures one obtains a paramagnetic phase while at low T one finds two ordered phases. All phase transitions appear to be of first-order type. For $J_2' < 0$ one obtains 120° valley order coexisting with spin-ferromagnetic order, while for $J_2' > 0$ a state with 120° valley order and coplanar 120° spin order in one of the two valleys is realized. The transition temperature between the two phases follows the analytically estimated slope $T_c \approx 8.21 J_2'$ (white dashed line in panel (b)). Panel (b): The spin-ferromagnetic order supports a finite spin-chirality $|\chi^+ - \chi^-|$ at finite T. Panel (c): As the spins order coplanar in one valley but remain ferromagnetic in the other, τ_z develops a finite expectation value.

leading order in $1/M$, where M is set to its physical value, $M = 1$ at the end of the calculation, corresponding to one localized electron per site. In the classical limit, at low-T deviations from mean-field are small, which allows to make quantitative predictions based on spin wave theory.

The naive spin-wave calculation in the classical limit predicts a divergent result reflecting the ground-state degeneracy of the $T = 0$ state. This degeneracy is lifted by the order-by-disorder mechanism discussed above which provides a mass linear in T to the chirality-mode. Taking this higher-order (in $1/M$) effect into account we obtain

$$\langle \hat{\chi}^+ - \hat{\chi}^- \rangle \approx \pm 0.22 \frac{T}{J_2} \ln \left[\sqrt{T_0/T} \right] , \qquad (12)$$

in perfect agreement with the numerical data, see inset of figure 4(b). The prefactor is fixed by our analytical results, see appendix E, and the only fitting parameter is T_0. We expect that such a non-analytic T dependence is generic for classical systems with a degenerate ground-state manifold where a ground state of the manifold is selected by thermal fluctuations. Thus some 'pseudo Goldstone modes' obtain masses linear in T, leading to non-analytic $T \log 1/T$ corrections in spatial dimension $d = 2$ or a $c_1 T + c_2 T^{3/2}$ correction in spatial dimension $d = 3$ for observables coupling to the mode, see appendix E.

The sign in equation (12) is related to the spontaneous breaking of the $\mathbb{Z}_2$ symmetry, $e^{i\pi\tau_x/2} = i\tau_x$, which maps χ^+ to χ^-. Therefore, $\langle \hat{\chi}^+ - \hat{\chi}^- \rangle$ can be used, at $T > 0$, as an Ising order parameter of this symmetry. The extremely sharp rise of $\langle \hat{\chi}^+ - \hat{\chi}^- \rangle$ at the phase transition, see figure 4(b), is both consistent with an Ising phase transition, $\langle \hat{\chi}^+ - \hat{\chi}^- \rangle \sim (T_c - T)^{1/8}$, or a first-order transition, see appendix F.

In figure 5 we show the phase diagram of the $J_2 - J_2'$ model as a function of temperature T and coupling J_2'. At $T = 0$, this simply reproduces the mean-field result. While for $J_2' < 0$ a ferromagnetic spin-order coexists with a 120° valley order, one obtains a coplanar spin order in one of the two valley sectors for $J_2' > 0$. Thus the valley symmetry is spontaneously broken in this phase, leading to a finite expectation value for τ_z, see figure 5(c). Numerically, we find that the phase transition into the spin-coplanar phase at $J_2' > 0$ both as a function of T or J_2' is always of first order; an analysis of the energy distribution is given in appendix F. At low T, the first-order phase transition separating the two ordered phases has a linear slope, $T_c \propto J_2'$. This arises because at $J_2' = 0$ the spin-ferromagnetic state gains energy linear in T due to the order-by-disorder mechanism described above. This linear-in-T energy gain competes with a linear-in-J_2' energy gain of the spin-coplanar phase, figure 6(b), which arises because J_2' selects at $T = 0$ one of the states from the ground-state manifold of H_0. Analytically, we obtain from this argument $T_c \approx 8.21 J_2'$, which quantitatively explains the numerically observed slope, as shown in figure 5(b). As discussed above, the finite-T transition from the paramagnetic into spin ferromagnetic phase is accompanied by a $\mathbb{Z}_2$ symmetry breaking.

For all considered values of J_2' the specific heat shows a low temperature saturation of $c_v(T \to 0) = 3$, indicating that both ordered states in figure 5 feature six harmonic modes [61] per site as expected for an $SU(4)$ model locally described by 6 parameters as discussed above.

5. Quantum fluctuations

Above, we discussed the effect of thermal fluctuations and showed that at low T an $SU(4)$ spin-wave calculation in the classical regime reproduces the main numerical findings qualitatively and quantitatively including the order-by-disorder mechanism and non-analytic T dependences arising from pseudo Goldstone modes. While the $SU(4)$ spin-wave theory becomes exact in the classical case for $T \to 0$, this is not the case in the quantum model, where quantum fluctuations in the ground state can be large. $SU(4)$

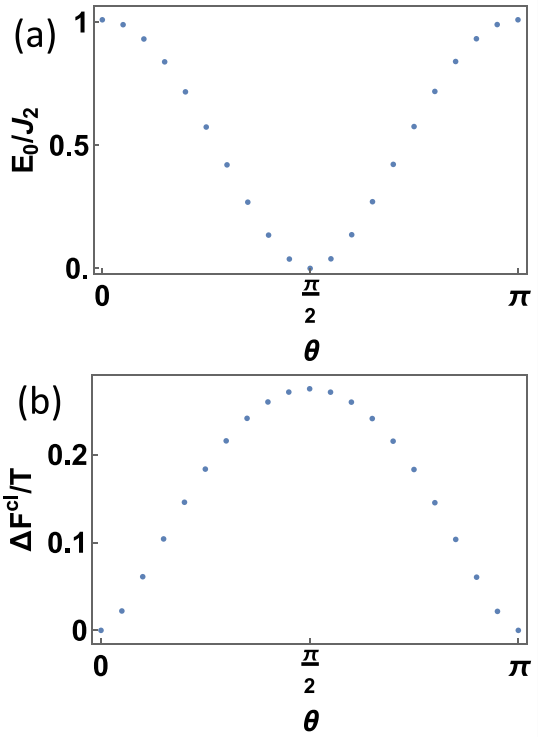

Figure 6. Order-by-disorder mechanisms. (a) Ground-state energy per site computed from $SU(4)$ spin-wave theory as function of θ, parameterizing the opening angle of valley-projected spins in the three sublattices. By the quantum order-by-disorder mechanism, a state with the an opening angle $\theta = \pi/2$ (i.e. the spin-coplanar 120° order in one of the two valleys) is selected from the mean-field ground-state manifold. (b) In the classical model, the free energy obtains at low T a correction linear in T from thermal fluctuations. In contrast with the quantum order-by-disorder mechanism, the thermal order-by-disorder leads to the selection of the spin ferromagnetic order in both of the valley sectors ($\theta = 0$ or π).

spin wave theory only becomes exact in a large M limit, see appendix E but we expect that qualitative features of ordered phases (in contrast to spin-liquid phases) are well captured by this approach.

In figure 6(a), we show the corrections due to quantum fluctuations to the ground-state energy of H_0, equation (11), as a function of the spin-opening angle θ. The state with $\theta = \pi/2$, i.e. a coplanar 120° order of the spins in one of the valley sectors, is selected by quantum fluctuations. In contrast, as discussed above, thermal fluctuations select spin-ferromagnetic order ($\theta = 0$ or π). Thus, our system is one of the rare cases where quantum and classical fluctuations select very different types of ground states. As we show in appendix E, this arises, technically, because classically a state is selected where the *geometric* average of the excitation energies $E_{\boldsymbol{k},n}$ is lowest, while quantum fluctuations select the state with the lowest *arithmetic* average of all $E_{\boldsymbol{k},n}$. While in most systems the two averages show the same qualitative behavior, this is not the case in our system.

How will the quantum fluctuations modify the ground-state phase diagrams shown in figure 3? The main effect of quantum fluctuations is that they break the degeneracy of mean-field ground state of H_0. As shown in figure 6(a), the ground-state energy obtains a θ dependence. An almost identical θ dependence can be obtained in the purely classical model by adding a J_2' to the Hamiltonian with $J_2' \approx 0.45 J_2$. Thus, we speculate that the quantum fluctuations have a similar effect on the phase diagram as increasing J_2' within mean-field theory. This procedure is well-controlled in an $1/M$ expansion, see appendix E: for large M, quantum corrections of order $1/M$ can be fully compensated by a shift of J_2' by $-0.45 J_2/M$ (up to corrections of order $1/M^2$).

Thus, we expect that the main effect of quantum fluctuations will be that in figures 3(b) and (c) the phase boundaries are shifted along the y direction, most likely accompanied by a rounding of the sharp kink where the phases meet. This extra rounding would be a $1/M^2$ effect, which is more difficult to calculate.

6. Summary: phases and the impact of fluctuations

We briefly summarize the obtained phases and the impact of quantum and thermal fluctuations on them. The peculiar and diverse phase diagrams of figure 3 originate a variant of the Kugel–Khomskii model, H_0 (equation (11)), where the mean-field ground states are highly degenerate. The mean-field ground states of H_0 are parameterized by two different order parameters: a discrete order parameter $\langle \boldsymbol{\mu}^{n=1,2} \rangle$ and a continuous order parameter, the valley-projected magnetization $\langle P^{\pm} \boldsymbol{\sigma} \rangle$. The ground states have a three-site unit-cell where $\langle \boldsymbol{\mu}_m^n \rangle$ have the norm 1, and show 120° order such that $\langle \boldsymbol{\mu}_{m_1}^n \rangle \cdot \langle \boldsymbol{\mu}_{m_2}^n \rangle = \cos(2\pi/3)$ for neighboring sites. There coexist two different types of 120° order, which have the opposite circulation direction of $\langle \boldsymbol{\mu}^n \rangle$ on a triangle. The transition between the two of them is of first-order, indicated by the dashed lines of figure 3.

A more interesting property of the ground states of H_0 is defined on $\langle P^{\pm} \boldsymbol{\sigma} \rangle$. In one of the two valleys, $\langle P^{\pm} \boldsymbol{\sigma} \rangle$ is always ferromagnetic, but in the other valley, $\langle P_m^{\pm} \boldsymbol{\sigma}_m \rangle$ on the three sublattices form arbitrary opening angle θ with $0 \leqslant \theta \leqslant \pi$; ferromagnetic spin-order ($\theta = 0$ or π), 120° coplanar spin order ($\theta = \pi/2$), and non-coplanar spin order ($\theta \neq 0, \pi/2, \pi$) with a finite spin chirality, see appendix D for more details. Those highly rich ground state manifold allows to possess a wealth of phase diagrams as shown in figure 3. When small perturbations are added on H_0, a ground state is selected from the ground state manifold of H_0 to minimize the energy. For example, the positive J_2' term in equation (10) favors the ferromagnetic spin order while the negative J_2' term favors the coplanar spin order, see figures 3(b) and (c).

The degeneracy of the mean-field ground state of H_0 is, however, lifted by quantum and thermal

fluctuations. By the order-by-disorder mechanism, quantum fluctuations favor the coplanar spin order, while thermal fluctuations favor the ferromagnetic spin order. Furthermore, the effect of the fluctuations on the spin chirality differs by the spin order of the ground state. While the coplanar spin order has a vanishing chirality against the fluctuations, the ferromagnetic order easily obtains a finite chirality from the fluctuations (e.g. see figure 5(b) for a finite chirality induced by the thermal fluctuations when $J_2' < 0$). In the classical limit, this fluctuation effect on the ferromagnetic order is enhanced due to the coupling to a pseudo Goldstone mode associated with opening angle θ.

7. Conclusions

Our study reveals that one of the simplest feasible moiré systems, a single layer of graphene on an insulating substrate, can exhibit surprisingly rich physics. Ultra-flat bands generating localized modes coexist with a network of chiral 1D channels where electrons move very fast with a speed set by the Fermi velocity of graphene. A main advantage of such large-unit-cell system is that one can tune the electron density by external gates. Insulating substrates with a honeycomb structure provide an ideal realization of our model but as discussed in appendix C, a wide range of different substrate with triangular symmetry, including AB stacked graphene, can also be used.

Different types of localized modes with spin-, valley- and orbital degrees of freedom can be realized depending on how many electrons are loaded into the local level and the quantum numbers of the localized states, fixed by the representation of the relevant dicyclic group. The chiral nature of the channels connecting the localized modes gives rise to characteristic chiral- and non-chiral interactions. We expect that a wealth of different phases with commensurate and incommensurate spin-, valley- and orbital order can be realized.

As an example, we studied one such model, focusing on commensurate order stabilized by two- and three spin interactions. We use mean-field theory, an $SU(4)$ spin-wave theory both in the classical and quantum regime, and Monte Carlo simulations of a semi-classical model. By tuning gate voltages one can control k_F and thus the effective interactions. One can, for example, tune parameters along the yellow line shown in figure 3(b). This triggers a transition from a coplanar phase with ferromagnetic spin and 120° valley order into a non-coplanar phase characterized by a peculiar coexistence of three different types of order: ferromagnetic spin order in one valley, non-coplanar chiral spin order in the other valley, and 120° order in remaining spin and valley-mixed degrees of freedom. Such a transition between different orders can be observed in experiments by tuning gate voltage. The most direct way to probe different types of order experimentally, is probably to use a magnetic scanning tunneling microscopy which is not only sensitive to the magnetic order but also to valley order as has been, e.g. discussed in [62]. Another exciting possibility is to probe spin chirality using optical means (e.g. [63]).

The peculiar form of the mean-field phase diagrams, where tiny perturbations can profoundly change the ground state, is governed by the proximity to a variant of the Kugel–Khomskii model, H_0, where the mean-field ground state is highly degenerate. For example, the tiniest chiral interactions arising from 3-spin interactions mediated by the chiral electronic channels, induce a state with a huge spin-chirality in one of the valleys. The degeneracy of the mean-field ground state of H_0 is, however, lifted by quantum and thermal fluctuations. While in most systems, quantum and thermal fluctuations stabilize the same type of order by such an order-by-disorder mechanism, this is not the case in our model where quantum fluctuations prefer coplanar spin-order, while classical fluctuations favor ferromagnetic spin order on top of a 120° valley order. The ferromagnetic spin order is, however, highly unconventional. Due to the coupling of spin- and valley degrees of freedom, quantum or thermal fluctuations around the spin-ferromagnetic state are *always* chiral with a finite spin-chirality. In the classical limit, this fluctuation effect is enhanced, equation (12), due to the coupling to a pseudo Goldstone mode characteristic for the classical order-by-disorder mechanism.

Our results on quantum fluctuations are based on a spin-wave calculation, which formally becomes exact in a large M limit. As $M = 1$, this result remains speculative. An alternative scenario is that for $M = 1$ quantum fluctuations around the highly degenerate mean-field state induce a spin-valley entangled quantum liquid. It would be interesting to test these very different scenarios in future numerical studies. Furthermore, we expect that the system will host many more commensurate and incommensurate phases and, potentially, quantum liquids, when other localized modes and different electronic fillings are considered.

Data availability statement

All data that support the findings of this study are included within the article (and any supplementary files).

Acknowledgments

We thank Martin Zirnbauer, Guo-Yi Zhu, Ciarán Hickey, Shahal Ilani, Nick Bultinck, Johannes Hofmann, Peter Cha and Hongki Min for useful discussions. Financial support of the Deutsche Forschungsgemeinschaft (DFG, German Research Foundation) within CRC1238 (Project Number

277146847, C02 and C04) and CRC183 (Project Number 277101999, A01 and A04) is acknowledged. Jeyong Park also acknowledges BCGS (Bonn-Cologne Graduate School) and ML4Q (Matter and Light for Quantum Computing) for support. The numerical simulations were performed on the Noctua 2 cluster at the Paderborn Center for Parallel Computing (PC2) and the CHEOPS cluster at RRZK Cologne.

Note added: Recently, a preprint by Wittig *et al* was published on ArXiv [64] that also considers localized states coupled to a network of chiral modes in the TBG subject to an interlayer bias.

Appendix A. Symmetry analysis for the network model

In this appendix, we discuss the symmetry of the moiré system considered in the main text, and identify the form of the coupling $\hat{w}$ and $\hat{\lambda}$ (equation (4)) using a symmetry analysis.

A.1. Symmetry

The underlying lattice or discrete symmetries of our moiré model are the moiré translation, the 120° rotation (C_3), the mirror (M_y) with respect to the y axis, the inversion ($\mathcal{I}$), and the time reversal symmetry ($\mathcal{T}$) and combinations thereof. Since the moiré potential varies smoothly so that the large-momentum transfer is highly suppressed, it is a good approximation to consider the two valley sectors separately. Therefore, we only consider the valley-conserving symmetries generated by C_3, M_y, and $\mathcal{TI}$, in the following.

The underlying lattice symmetry group is the dehedral group D_3 with C_3 and M_y. More precisely, in order to deal with the spinor wave function properly, one has to take into account a minus sign under 2π rotation, and therefore consider the dicyclic group Dic_3, which extends D_3. The character table of Dic_3 is as follows:

Dic_3	**A**	**B**	**C**	**D**	**E**	**F**
ρ_1	1	1	1	1	1	1
ρ_2	1	1	1	−1	−1	1
ρ_3	1	−1	−1	i	$-i$	1
ρ_4	1	−1	−1	$-i$	i	1
ρ_5	2	2	−1	0	0	−1
ρ_6	2	−2	1	0	0	−1

with the 6 irreducible representations $\rho_{j=1,\ldots,6}$ and the equivalent classes $\mathbf{A},\mathbf{B},\mathbf{C},\mathbf{D},\mathbf{E},\mathbf{F}$ which are given by

$$\mathbf{A}\equiv\{1\},\ \mathbf{B}\equiv\{C_3^3\},\ \mathbf{C}\equiv\{C_3,C_3^5\},$$
$$\mathbf{D}\equiv\{M_yC_3,M_yC_3^3,M_yC_3^5\},\ \mathbf{E}\equiv\{M_y,M_yC_3^2,M_yC_3^4\},$$
$$\mathbf{F}\equiv\{C_3^2,C_3^4\}.$$

For states with one electron per mode, only three of the representations, ρ_3, ρ_4, ρ_6, are relevant since the condition $C_3^3=-1$ should be fulfilled for the spinor wave functions. While ρ_3 and ρ_4 are 1D representations, ρ_6 is a two-dimensional representation.

As shown in figure 1, the moiré system is effectively described by the network model where localized states form at the junction of three 1D channels (for each valley) and are weakly coupled to the channels. Below, employing a symmetry analysis, we shall find the form of the inter-channel coupling $\hat{w}$ and the coupling of 1D channels to localized states $\hat{\lambda}$ (equation (4)).

A.2. Localized modes

Localized states can be labeled by representation $\rho_{j=3,4,6}$ of the group Dic_3. From the character table, one can find relevant matrices for the transformation C_3 and M_y in each of the representations: $C_3^{\rho_3}=-1, C_3^{\rho_4}=-1, C_3^{\rho_6}=e^{i\pi\sigma_z/3}$ and $M_y^{\rho_3}=-i,\ M_y^{\rho_4}=i, M_y^{\rho_6}=e^{i\pi\sigma_y/2}$, respectively. A simple way to identify the symmetry of a given localized state from the band-structure calculation is to analyze the symmetry properties of the eigenfunction of flat bands at the Γ point. For each of the three representations we find examples in our band structure calculations, see figure 2(c) of the main text.

A.3. 1D channels

From scaling, one finds that the width of the 1D channels is given by $d_{1\mathrm{D}}\sim(vL/u_s)^{1/2}$ with $d_{1\mathrm{D}}\ll L$ for $u_s\gg vG$. $d_{1\mathrm{D}}\ll L$ renders that the coupling of 1D channels being far apart is highly suppressed, and thus it is a good approximation to only consider the coupling of the neighboring channels at the junction. The symmetry properties are determined by the spinor structure of the eigenfunctions. The three channels at the junction are related to each other by a 120° rotation matrix, $C_3^{1\mathrm{D}}$, and the mirror transformation matrix, $M_y^{1\mathrm{D}}$, e.g. for the K valley, written by

$$C_3^{1\mathrm{D}}=\begin{pmatrix}0&0&-1\\1&0&0\\0&1&0\end{pmatrix},\ M_y^{1\mathrm{D}}=\begin{pmatrix}-i&0&0\\0&0&i\\0&i&0\end{pmatrix}. \tag{A1}$$

For the K' valley, the mirror transformation matrix has an extra overall minus sign as K and K' are related by time-reversal and thus by complex conjugation. The relative minus sign in one of the matrix elements of C_3 and M_y reflects the fact that the 2π rotation preinor wave function gets a minus sign. Also $(\mathcal{IT})^{1D} = C\mathbb{1}_3$, where C is the complex conjugation and $\mathbb{1}_3$ is the 3×3 unit matrix. The inter-channel tunneling H_w is written as

$$H_w = \sum_{\text{crossing at } \boldsymbol{R}_m} \hat{w}_{ii'} \Psi^{\dagger}_{n,i,\alpha,\sigma}(\rho_{n,i,m}) \Psi_{n',i',\alpha,\sigma}(\rho_{n',i',m}). \tag{A2}$$

By imposing the symmetry constraints, $\hat{w} = (C_3^{1D})^{\dagger}\hat{w}C_3^{1D}$, $\hat{w} = (M_y^{1D})^{\dagger}\hat{w}M_y^{1D}$, and $\hat{w} = ((\mathcal{IT})^{1D})^{\dagger}\hat{w}(\mathcal{IT})^{1D}$, one can obtain $\hat{w}$, parameterized by a single real parameter w as

$$\hat{w} = wL \begin{pmatrix} 0 & 1 & -1 \\ 1 & 0 & 1 \\ -1 & 1 & 0 \end{pmatrix}. \tag{A3}$$

The size of moiré unit cell, L, is used such that w has units of energy.

A.4. Coupling between localized and propagating modes

The coupling of 1D channels to localized modes, equation (4), depends on to which representation of Dic_3 the localized mode belongs. Similarly to the $\hat{w}$ matrix, this coupling matrix $\hat{\lambda}$ can be obtained by the symmetry constraints, $\hat{\lambda} = (C_3^{\rho_j})^{\dagger}\hat{\lambda}C_3^{1D}$, $\hat{\lambda} = (M_y^{\rho_j})^{\dagger}\hat{\lambda}M_y^{1D}$, and $\hat{\lambda} = ((\mathcal{IT})^{\rho_j})^{\dagger}\hat{\lambda}(\mathcal{IT})^{1D}$, for each of the representation $j = 3, 4, 6$. For the K valley, it is given by

$$H_\lambda = \sum_{\text{crossing at } \boldsymbol{R}_m} \hat{\lambda}_{ij} d^{\dagger}_{m,\alpha,\sigma,j} \Psi_{n,i,\alpha,\sigma}(\rho_{n,i,m}) + h.c.,$$

$$\hat{\lambda} = \lambda \frac{\sqrt{L}}{\sqrt{3}} \begin{cases} (1,-1,1) & \rho_3 \text{ rep} \\ (0,0,0) & \rho_4 \text{ rep} \\ \begin{pmatrix} 1 & e^{i\pi/3} & e^{2i\pi/3} \\ -i & -ie^{-i\pi/3} & -ie^{-2i\pi/3} \end{pmatrix} & \rho_6 \text{ rep.} \end{cases} \tag{A4}$$

Interestingly, the localized modes in the ρ_4 representation do not couple to the closest 1D channels at all. This vanishing coupling can be understood by the symmetry of the system. For example, let us consider the coupling of a localized mode in the ρ_4 representation to the neighboring channel propagating in the y direction. While the localized mode has the eigenvalue i under the mirror transformation M_y, the channel has the eigenvalue $-i$. It implies that the coupling matrix $\hat{\lambda}$ has to have an extra minus sign under M_y, and therefore has to vanish. The same argument can be applied to the two other neighboring channels with the symmetry transformation M_yC_3, and $M_yC_3^2$. Nevertheless, tunneling to channels further away are still possible but exponentially suppressed in the ratio of potential and vG as $e^{-L/d_{1D}} \sim e^{-(u_sL/v)^{1/2}}$.

The coupling matrices for the K' valley can be obtained by time reversal, which implies that the time-reversed partner of ρ_3 and ρ_4 have an identical coupling matrix $\hat{\lambda}$. Formally, under time-reversal ρ_3 maps to ρ_4 but this effect is compensated because also in equation (A4) the entries for ρ_3 and ρ_4 are exchanged when one switches from K to K'. The matrix $\hat{\lambda}$ for ρ_6 in the K' valley is obtained by complex conjugation of $\hat{\lambda}$.

Appendix B. Effective Hamiltonian in momentum space

In this appendix, we construct an effective Hamiltonian for the network model in momentum space and show that the band structure obtained from the diagonalization of the moiré potential model, equation (1), is nicely fitted by the band structure obtained from this effective model.

As shown in figure 2(c) for the band structure in the main text (also the blue solid curves in figure 7), the inter-channel coupling and the coupling of 1D channels to localized states are very weak. For example, a blowup of the band structure near the Γ point (indicated by the black circle) in figure 7 shows that a level-repulsion of the three 1D channels is an order of hundreds of μeV. Such weak couplings (i.e. $w, \lambda \ll vG$) allow us to construct an effective Hamiltonian from equations (3) and (4). Depending on the number of localized modes, N_{loc}, within the energy window of $\epsilon \in [-vG/2, vG/2]$ near the chemical potential, this effective Hamiltonian $H_{\text{eff}}(k_x, k_y)$ for a given valley can be described by a $(3+N_{\text{loc}}) \times (3+N_{\text{loc}})$ matrix for each momentum. For example, the band structure for the K valley shown in figure 2(c) can be reproduced with high precision by the 7×7 matrix, given by

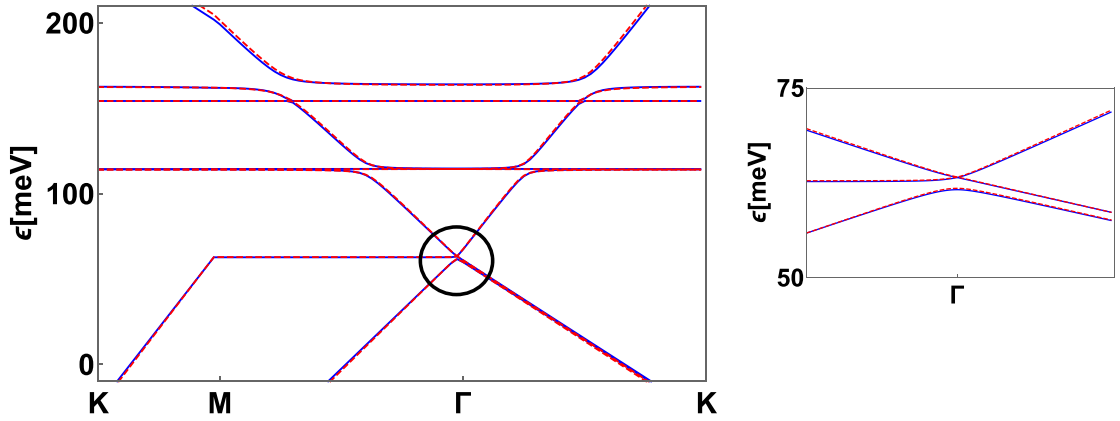

Figure 7. Comparison of two band structures. Left: The band structure (blue solid curves) obtained from diagonalizing the original moiré potential model, equation (1), and the band structure (red dashed curves) using the effective Hamiltonian, equation (B1). The parameters of equation (B1) can be obtained by fitting the blue solid curves; $w = 0.2$ meV, $\lambda_6 = 4.3$ meV, $\lambda_3 = 11.3$ meV, $\epsilon_{1D} = 63.4$ meV, $\epsilon_6 = 114$ meV, $\epsilon_4 = 154$ meV, and $\epsilon_3 = 162$ meV. Those band structures match remarkably, confirming the validity of our network model. For the blue curves, we have used the parameters, $u_{AA} = u_{BB} = 0$ and $u_{AB} = u_{BA} = \frac{8\pi v}{\sqrt{3}L}$. Right: a blowup of the band structures near the Γ point (indicated by the black circle) where the three propagating bands meet. Weak level repulsion between the three bands is clearly shown, not visible in the left band structure.

$$H_{\text{eff}}(k_x,k_y) = \begin{pmatrix} -vk_y+\epsilon_{1D} & w & -w & \frac{\lambda_6}{\sqrt{3}} & i\frac{\lambda_6}{\sqrt{3}} & \frac{\lambda_3}{\sqrt{3}} & 0 \\ w & -\frac{v}{2}\left(\sqrt{3}k_x-k_y\right)+\epsilon_{1D} & w & \frac{\lambda_6}{\sqrt{3}}e^{-i\frac{\pi}{3}} & i\frac{\lambda_6}{\sqrt{3}}e^{i\frac{\pi}{3}} & -\frac{\lambda_3}{\sqrt{3}} & 0 \\ -w & w & \frac{v}{2}\left(\sqrt{3}k_x+k_y\right)+\epsilon_{1D} & \frac{\lambda_6}{\sqrt{3}}e^{-2i\frac{\pi}{3}} & i\frac{\lambda_6}{\sqrt{3}}e^{2i\frac{\pi}{3}} & \frac{\lambda_3}{\sqrt{3}} & 0 \\ \frac{\lambda_6}{\sqrt{3}} & \frac{\lambda_6}{\sqrt{3}}e^{i\frac{\pi}{3}} & \frac{\lambda_6}{\sqrt{3}}e^{2i\frac{\pi}{3}} & \epsilon_6 & 0 & 0 & 0 \\ -i\frac{\lambda_6}{\sqrt{3}} & -i\frac{\lambda_6}{\sqrt{3}}e^{i\frac{\pi}{3}} & -i\frac{\lambda_6}{\sqrt{3}}e^{2i\frac{\pi}{3}} & 0 & \epsilon_6 & 0 & 0 \\ \frac{\lambda_3}{\sqrt{3}} & -\frac{\lambda_3}{\sqrt{3}} & \frac{\lambda_3}{\sqrt{3}} & 0 & 0 & \epsilon_3 & 0 \\ 0 & 0 & 0 & 0 & 0 & 0 & \epsilon_4 \end{pmatrix}. \tag{B1}$$

The first three rows and columns of this effective Hamiltonian describe the 1D channels propagating along the three directions, the 4- and 5th rows and columns describe degenerate localized states that belong to the ρ_6 representation with energy ε_6, and the 6 and 7th row and column correspond to localized states that belongs to the ρ_3 and ρ_4 representation with energy ε_3 and ε_4, respectively. As shown in equations (A2) and (A4), the form of the coupling terms is determined by the symmetry of the system and the representation of the localized states.

Figure 7 compares band structures obtained from two different Hamiltonians. The band structure plotted in blue dashed curves is numerically obtained from the diagonalization of the moiré model, equation (1). On the other hand, the band structure plotted in blue solid line is obtained from the 7×7 effective Hamiltonian in equation (B1) with the parameters of $w = 0.2$ meV, $\lambda_6 = 4.3$ meV, $\lambda_3 = 11.3$ meV, $\epsilon_{1D} = 63.4$ meV, $\epsilon_6 = 114$ meV, $\epsilon_4 = 154$ meV, and $\epsilon_3 = 162$ meV, which can be found by fitting to the blue dashed curves. Those band structures remarkably match well, including silent features. It confirms the validity of our network model.

Appendix C. Material realization—triangular substrates and TMBG

In the main text we considered an insulating substrate with a honeycomb structure like graphene. But main features of our model, the existence of regions where mass gap with alternating signs are induced into graphene, can also be generated with substrates of triangular symmetry for which many examples exist like hexagonal boron nitrite (h-BN). Also cutting a 3D cubic insulator at an (111) surface produces a substrate with triangular symmetry.

Within our effective model, equation (1), we can model such a substrate simply by removing the B-sublattice atoms from the lower layer by setting $u_{AB} = u_{BB} = 0$ in equation (2). This automatically leads to

an opening of the gap in the upper layer of opposite signs in the AA and BA regions. This has to be compared to the case of an hexagonal substrate where the gaps open in the AB and BA regions, see figure 2. Thus, to compare the two models directly, we should perform a shift by $\boldsymbol{r}_{AB}$, the vector connecting AA and AB regions. After such a shift, we obtain new parameters,

$$\tilde{u}_{AA} = \tilde{u}_{AB} = -u_{AA}, \quad \tilde{u}_{BB} = \tilde{u}_{BA} = -u_{BA}. \tag{C1}$$

Here the difference $u_{AA} - u_{BA}$ can be expected to be small in many systems. It describes the effect of corrugation: the distance of the two layers in the AA and BA regions are different, leading to different potentials. In the no-corrugation limit $u_{AA} = u_{BA}$, however, a perfect realization of our effective model is obtained with

$$\tilde{u}_{AA} = \tilde{u}_{AB} = \tilde{u}_{BB} = \tilde{u}_{BA} \tag{C2}$$

even for a substrate of with triangular symmetry.

To show that this idea also works in practice, we consider below a specific material, a twisted monolayer bilayer graphene (TMBG) subject to a perpendicular electric field. The TMBG is a van der Waals material where a monolayer graphene is stacked with relative twist on the top of a (non-twisted) AB-stacked bilayer graphene. This material has been recently realized in [32, 48]. While this system has a lower symmetry than the moiré potential model considered in the main part of the paper, equation (1), we show that it nevertheless approximately realizes key features of our model.

To investigate the system of TMBG with a small twist angle, we use a continuum model following the approach developed in [10]. We consider a monolayer graphene on the top of a AB-stacked bilayer graphene with relative twist angle ϕ. In the presence of a perpendicular electric field to the graphene layers, the monolayer graphene is subject to electrostatic potential $U/2$, while each layer of the bilayer graphene is subject to potential 0 and $-U/2$, respectively. In the sublattice basis, the low-energy physics for the monolayer graphene near the K point is captured by the Hamiltonian

$$H^0_{\mathrm{MG}} = v\boldsymbol{k}_{\phi/2} \cdot \boldsymbol{s} + \frac{U}{2}\mathbb{1} \tag{C3}$$

with the rotated momenta $\boldsymbol{k}_\theta \equiv R(\phi)\boldsymbol{k}$ by twist angle ϕ. Here $R(\phi)$ is the rotation matrix with angle ϕ, and $\boldsymbol{s} = (s_x, s_y)$ are the Pauli matrices acting on the sublattice space. The AB-stacked bilayer graphene can be described by the tight-binding Hamiltonian in basis of (A_1, B_1, A_2, B_2) with four atomic sites in the unit cell (1, 2 for the upper and lower layer, respectively),

$$H_{\mathrm{BG}} = \begin{pmatrix} 0 & v\pi^*_{-\phi/2} & -v_4\pi^*_{-\phi/2} & -v_3\pi_{-\phi/2} \\ v\pi_{-\phi/2} & \Delta & \gamma_1 & -v_4\pi^*_{-\phi/2} \\ -v_4\pi_{-\phi/2} & \gamma_1 & -\frac{U}{2}+\Delta & v\pi^*_{-\phi/2} \\ -v_3\pi^*_{-\phi/2} & -v_4\pi_{-\phi/2} & v\pi_{-\phi/2} & -\frac{U}{2} \end{pmatrix}. \tag{C4}$$

Here we linearize the tight-binding Hamiltonian expanding around K point to the linear order in momentum, and $\pi_\phi \equiv k_{\phi,x} + ik_{\phi,y}$. The intrinsic parameters of the bilayer graphene can be extracted from the density functional theory as $v = 8.45 \times 10^5$ m s^{-1}, $v_3 = 9.16 \times 10^4$ m s^{-1}, $v_4 = 4.47 \times 10^4$ m s^{-1}, $\Delta = 15$ meV, and $\gamma_1 = 361$ meV in [65]. The perpendicular electric field opens up a gap at K and K' points by $\sim|U|/2$.

The monolayer graphene is coupled with the upper layer of the bilayer graphene by the three 2×4 tunneling matrices

$$T(\boldsymbol{r}) = \sum_{j=1}^{3} e^{-i\boldsymbol{q}_j\cdot\boldsymbol{r}} T_j \tag{C5}$$

with

$$T_j = \begin{pmatrix} w_{AA} & e^{-i(j-1)\frac{2\pi}{3}} w_{AB} & 0 & 0 \\ e^{i(j-1)\frac{2\pi}{3}} w_{AB} & w_{AA} & 0 & 0 \end{pmatrix} \tag{C6}$$

with $j = 1, 2, 3$. Here we only take into account the three dominant interlayer tunneling processes [10]. $\boldsymbol{q}_j$ are the three dominant momentum transfers that correspond to the three interlayer tunneling processes; $\boldsymbol{q}_1 = K_\phi(0, -1)$, $\boldsymbol{q}_2 = K_\phi(\frac{\sqrt{3}}{2}, \frac{1}{2})$, $\boldsymbol{q}_3 = K_\phi(-\frac{\sqrt{3}}{2}, \frac{1}{2})$ with $K_\phi = 8\pi \sin(\phi/2)/(3a)$ and the graphene lattice constant a. The interlayer tunneling strengths $w_{AA}, w_{AB} > 0$ generically differ from each other due to the spatial modulation of the vertical distance between the monolayer and bilayer graphene (i.e. the corrugation effect). We neglect the coupling between the two valleys as the interlayer tunneling varies smoothly so that such a large momentum transfer between the valleys is exponentially suppressed.

The band structure of the Hamiltonian (equations (C3)–(C5)) can easily be obtained by exact diagonalization in momentum space. In figure 8 we show the resulting band structure for a realistic set of parameters and a small twist angle in comparison to the model discussed in the main text, equation (1).

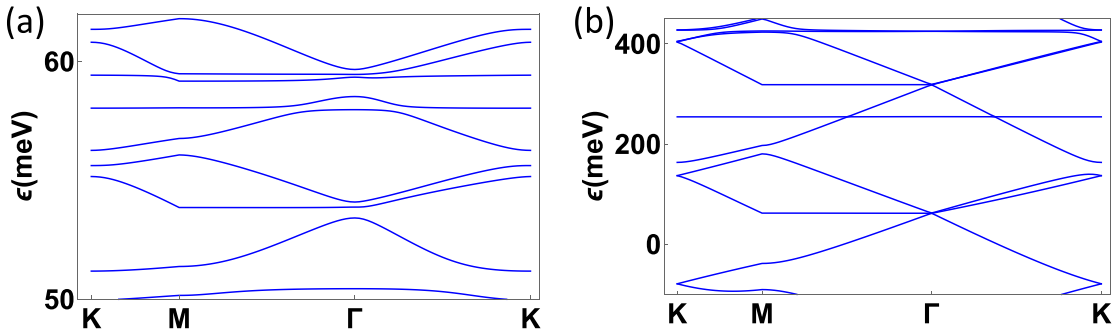

Figure 8. Comparison between a model for a twisted monolayer bilayer graphene with our potential model: Panel (a): Band structure of a twisted monolayer bilayer graphene in the presence of a weak corrugation with $w_{AA} = 88$ meV, $w_{AB} = 110$ meV. These band structures are obtained by numerically diagonalizing the Hamiltonian of equations (C3)–(C5) in momentum space. Although a degree of level repulsion and the magnitude of bandwidths are quite different, the band structure in panel (a) remarkably shows similarity to panel (b), a band structure of the potential model equation (1). Note that for panel (b) we have used different parameters of $u_{AA} = u_{BB} = -\frac{4\pi v}{3L}$ and $u_{AB} = u_{BA} = -\frac{4\pi v}{3L}$ from figure 2(c). Thus, the shape of panel (b) looks distinct from figure 2(c), but the band structure in panel (b) also exhibits 1D dispersing bands and flat bands. For panel (a) we have used the parameters $v = 8.45 \times 10^5$ m s^{-1}, $v_3 = 9.16 \times 10^4$ m s^{-1}, $v_4 = 4.47 \times 10^4$ m s^{-1}, $\Delta = 15$ meV, $\gamma_1 = 361$ meV, obtained from the density functional theory in [65]. We also have used the parameters of $U = -200$ meV and $\phi = 0.181°$.

The two results show a striking similarity. Also in TMBG for the chosen twist angle one can clearly identify the flat and the propagating bands. When comparing the two figures, one also sees directly, that the symmetry of TMBG is lower than in the moiré potential model (mirror symmetries are lacking). Symmetry-protected level crossings at the Γ and K points are absent in TMBG.

To obtain analytical insight why the two band structures are so similar, we have to map the TMBG model to our moiré potential model, equation (1). Analytically, this can be done assuming that the inter-layer tunneling is smaller than the bilayer gap $|U|/2$ (they are of similar size in the numerical example). Let us consider a state with energy E in the monolayer graphene. When E is inside the gap of the bilayer graphene, i.e. $\min(-U/2, 0) < E < \max(-U/2, 0)$ and $w_{AA}, w_{AB} < |U|/2$, the direct hybridization with bilayer graphene states is not allowed. Then, the leading correction on $H^0_{\rm MG}$ (equation (C3)) comes from the second-order process in tunneling, resulting in the following effective Hamiltonian of the monolayer graphene

$$H^{\rm eff}_{\rm MG} = H^0_{\rm MG} + \sum_{j=1,2,3} T_j \frac{1}{E - H_{\rm BG}} T_j^\dagger \,. \tag{C7}$$

Upon applying the Fourier transformation to the real space, the second term in equation (C9) becomes

$$\Delta H_{\rm MG}(\boldsymbol{r}, \boldsymbol{r}') = T(\boldsymbol{r}) g_{\rm BG}(\boldsymbol{r}, \boldsymbol{r}') T^\dagger(\boldsymbol{r}'), \tag{C8}$$

with the real space Green function $g_{\rm BG}(\boldsymbol{r}, \boldsymbol{r}') = (\frac{1}{E - H_{\rm BG}})(\boldsymbol{r}, \boldsymbol{r}')$ for the bilayer graphene. Due to the gap of the bilayer graphene, $g_{\rm BG}(\boldsymbol{r}, \boldsymbol{r}')$ exponentially decays in distance $|\boldsymbol{r} - \boldsymbol{r}'|$ over $\ell \sim 2v/|U|$. For sufficiently small twist angles, ℓ is much smaller than the size of the moiré unit cell L, and thus non-local effects are exponentially suppressed.

Under the assumption of $\ell \ll L$, we can focus on the local part $H^{\rm eff}_{\rm MG}(\boldsymbol{r}, \boldsymbol{r})$ of the effective Hamiltonian, which is written in a form

$$H^{\rm eff}_{\rm MG} = v(-i\nabla_{\boldsymbol{r}} - e\boldsymbol{A}(\boldsymbol{r})) \cdot \boldsymbol{s} + V^{\rm eff}_0(\boldsymbol{r}) \mathbb{1} + V^{\rm eff}_s(\boldsymbol{r}) s^z, \tag{C9}$$

where $V^{\rm eff}_0(\boldsymbol{r}) \approx \frac{1}{2}{\rm tr}[H_{\rm MG}(\boldsymbol{r}, \boldsymbol{r})]$, $V^{\rm eff}_s(\boldsymbol{r}) \approx \frac{1}{2}{\rm tr}[\sigma_z \cdot H_{\rm MG}(\boldsymbol{r}, \boldsymbol{r})]$ and an effective vector potential is obtained by setting $-ev\boldsymbol{A} = \frac{1}{2}{\rm tr}[(\sigma_x, \sigma_y) H_{\rm MG}(\boldsymbol{r}, \boldsymbol{r})]$. Here we assumed that ϕ is small, neglecting the ϕ-dependence in the first term of equation (C3). We have checked that the effective magnetic field $\boldsymbol{B} = \boldsymbol{\nabla} \times \boldsymbol{A}$ vanishes in every $\boldsymbol{r}$, and hence the vector potential $\boldsymbol{A}$ in equation (C9) can be gauged away. $V^{\rm eff}_0 = (V_A + V_B)/2$ and $V^{\rm eff}_s = (V_A - V_B)/2$ represent the effective uniform and staggered moiré potential onto the monolayer graphene, which is induced by the second-order process in the inter-layer tunneling. From the straightforward calculation of equation (C9) using equation (C5), one can show that V_A and V_B take the form

$$V_A(\boldsymbol{r}) = \frac{\overline{V}_0 + \overline{V}_s}{2} + \sum_{\beta=A,B} \sum_{i=1}^{6} u_{A\beta} e^{i\boldsymbol{G}_i \cdot (\boldsymbol{r} - \boldsymbol{r}_{A\beta})}$$
$$V_B(\boldsymbol{r}) = \frac{\overline{V}_0 - \overline{V}_s}{2} + \sum_{\beta=A,B} \sum_{i=1}^{6} u_{B\beta} e^{i\boldsymbol{G}_i \cdot (\boldsymbol{r} - \boldsymbol{r}_{B\beta})}\,, \tag{C10}$$

with the six smallest moiré reciprocal lattice vectors $\boldsymbol{G}_i$ and $\boldsymbol{r}_{AA} = \boldsymbol{r}_{BB} = 0$, $\boldsymbol{r}_{AB} = -\boldsymbol{r}_{BA} = (\frac{\sqrt{3}L}{6}, \frac{L}{2})$, see figure 2(a). $\overline{V}_0$ and $\overline{V}_s$ denote the constant part of the effective uniform and stagger potentials, respectively. The parameters $u_{\beta\beta'}$, $\overline{V}_0$, and $\overline{V}_s$ in equation (C10) are written in terms of the parameters of the TMBG as

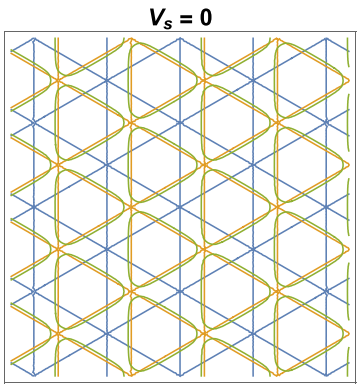

Figure 9. The effect of the inversion symmetry breaking: Lines along which the mass gap vanishes, i.e. $V_s(\boldsymbol{r}) = (V_A + V_B)/2 = 0$, see equation (C10). The blue lines are drawn for the case to preserve the inversion symmetry, i.e. $\gamma_1 = \Delta = 0$ and $w_{AA} = w_{AB}$ to share the same symmetries discussed in the main text. The orange lines are drawn for the case with $\gamma_1 \to \infty$ to strongly break the inversion symmetry. Compared with the inversion symmetric case (blue lines), the straight lines are shifted by $\boldsymbol{r} \to \boldsymbol{r} + \boldsymbol{r}_{AB}$ in which the symmetries discussed in appendix A are fully restored. The green lines are drawn with the experimental parameters of $\gamma_1 = 361$ meV, $\Delta = 15$ meV, $U = -200$ meV, $w_{AA} = 88$ meV, and $w_{AB} = 110$ meV. Apart from the bending near the crossing points, the lines remain straight. For those plots, E is set to $-U/4$, the middle of the gap of the bilayer graphene.

$$
\begin{aligned}
u_{AA} &= -\frac{4w_{AA}^2}{U}, \quad u_{BA} = -\frac{4w_{AB}^2}{U}, \\
u_{AB} &= -\frac{4w_{AB}^2(U-4\Delta)}{16(\gamma_1^2-\Delta^2)+U^2}, \\
u_{BB} &= -\frac{4w_{AA}^2(U-4\Delta)}{16(\gamma_1^2-\Delta^2)+U^2}, \\
\overline{V}_s &= \frac{24(w_{AB}^2-w_{AA}^2)(4\gamma_1^2+(U-4\Delta)\Delta)}{U(16(\gamma_1^2-\Delta^2)+U^2)}, \\
\overline{V}_0 &= -\frac{12(w_{AB}^2+w_{AA}^2)(8(\gamma_1^2-\Delta^2)+U^2-2U\Delta)}{U(16(\gamma_1^2-\Delta^2)+U^2)}.
\end{aligned}
\tag{C11}
$$

Here E is set to $-U/4$, deep in the gap of the bilayer graphene. As γ_1 is relatively large, we find that $u_{AB} \approx 3.8$ meV, $u_{BA} \approx 5.9$ meV can be neglected compared to $u_{AA} \approx 155$ meV and $u_{AB} \approx 242$ meV as anticipated above. The difference of u_{AA}, u_{AB} is, however, substantial as in this system corrugation effects are enhanced as the tunnel coupling of the layers enters quadratically in equation (C11). Nevertheless, the model approximately realizes the physics discussed in the main text which largely relies on the fact that $V_s^{\mathrm{eff}}(\boldsymbol{r})$ (and thus the local mass gap) vanishes along lines in real-space which lead both to propagating 1D modes running parallel to them and localized modes at their crossing point. Therefore, we plot in figure 9 the contours of $V_s(\boldsymbol{r}) = 0$ for realistic parameters of TMBG (green lines). These contours deviate strongly from the contours of our original model drawn in blue which are obtained for $u_{AA} = u_{BB}$ and $u_{AB} = u_{BA}$. As discussed above, the models are only expected to match after a shift of the potential by $\boldsymbol{r}_{AB}$, which leads to the orange lines in figure 9 which are remarkably close to the ones derived from the realistic model of TMBG. This provides an analytical justification of the numerical results of figure 8 and corroborates our argument that approximate realizations of our effective model can be expected even for lower-symmetry substrates with triangular lattices.

Appendix D. Mean-field phase diagram

In this appendix, we discuss the mean-field phase diagram of the Hamiltonian, equation (10), given by

$$
\begin{aligned}
H_{\mathrm{sv}} = J_2 \sum_{\langle m_1 \to m_2 \rangle_c} (1 + \boldsymbol{\sigma}_{m_1} \cdot \boldsymbol{\sigma}_{m_2})(e^{i\varphi}\tau_{m_1}^+ \tau_{m_2}^- + h.c.) + J_3 \sum_{p=\triangleright/\triangleleft,(m_1,m_2,m_3)_p} (-1)^p \boldsymbol{\sigma}_{m_1} \cdot (\boldsymbol{\sigma}_{m_2} \times \boldsymbol{\sigma}_{m_3}) \left(\prod_{i=1}^3 P_{m_i}^+ - \prod_{i=1}^3 P_{m_i}^- \right) \\
+ J_2' \sum_{\langle m_1, m_2 \rangle_c} (1 + \boldsymbol{\sigma}_{m_1} \cdot \boldsymbol{\sigma}_{m_2})(1 + \tau_{m_1}^z \tau_{m_2}^z) \ .
\end{aligned}
\tag{D1}
$$

Compared with the Hamiltonians (equations (7)–(9)) obtained from a perturbation theory in J and w, the Hamiltonian contains only the nearest neighbor interactions. The continuous symmetries of H_{sv} are $U(1) \times SU(2) \times SU(2)$ generated by τ^z, $P^+\boldsymbol{\sigma}$ and $P^-\boldsymbol{\sigma}$. Assuming that the filling of the localized states

is unity, the states on the $SU(4)$ space are spanned by a 4-component complex vector. In this basis, we solve the self-consistent mean-field equations iteratively with the fixed unit cell. We use 4 different unit cells with one-, two-, three-, four-sublattices. We find that either a one-sublattice or a three-sublattice solution has the lowest energy. Therefore we consider only these cases in the following.

The model is parametrized by 3 dimensionless parameters J_3/J_2, J_2'/J_2 and φ. Experimentally, we expect $|J_3/J_2|, |J_2'/J_2| \ll 1$ while φ can take arbitrarily large values. The parameter φ can be viewed as an Aharonov–Bohm phase acquired by a particle with charge τ^z moving along a side of the triangular loop. As 3φ is the total phase accumulated along the triangular loop, it is possible to use a transformation to change the total phase by 2π which is equivalent to a change of φ by $n2\pi/3$, $n \in \mathbb{Z}$. This is achieved by doing τ^z rotations of the spins on the A, B, C (see the inset of figure 3) by 0, $2\pi/3$, $4\pi/3$

$$\varphi \to \varphi + \frac{2\pi}{3},\ \boldsymbol{\tau}_{\mathrm{A}} \to \boldsymbol{\tau}_{\mathrm{A}},\ \boldsymbol{\tau}_{\mathrm{B}} \to e^{i\tau_{\mathrm{B}}^z \frac{2\pi}{3}} \boldsymbol{\tau}_{\mathrm{B}} e^{-i\tau_{\mathrm{B}}^z \frac{2\pi}{3}},$$
$$\boldsymbol{\tau}_{\mathrm{C}} \to e^{i\tau_{\mathrm{C}}^z \frac{4\pi}{3}} \boldsymbol{\tau}_{\mathrm{C}} e^{-i\tau_{\mathrm{C}}^z \frac{4\pi}{3}}. \tag{D2}$$

If one uses the Aharonov–Bohm analogy described above, this would be a gauge transformation. In our system, however, a rotation by τ^z changes the physical state. The transformation maps, for example, a ferromagnetic state obtained for $\varphi = \pi$ to a state with 120° order for $\varphi = \pm\pi/3$, see below.

As $J_2 > 0$ is the largest term, we first analyze the case $J_3 = J_2' = 0$. For $\varphi = 0$, the Hamiltonian, equation (D1), becomes a variant of the Kugel–Khomskii model [49]

$$H_0 = 2J_2 \sum_{\langle m_1 \to m_2 \rangle_c} (1 + \boldsymbol{\sigma}_{m_1} \cdot \boldsymbol{\sigma}_{m_2})(\tau_{m_1}^x \tau_{m_2}^x + \tau_{m_1}^y \tau_{m_2}^y)$$
$$= 2J_2 \sum_{\langle m_1 \to m_2 \rangle_c} \boldsymbol{\mu}_{m_1}^1 \cdot \boldsymbol{\mu}_{m_2}^1 + \boldsymbol{\mu}_{m_1}^2 \cdot \boldsymbol{\mu}_{m_2}^2, \tag{D3}$$

with the 4-component vectors given by $\boldsymbol{\mu}_m^1 = (\tau_m^x, \tau_m^y\sigma_m^x, \tau_m^y\sigma_m^y, \tau_m^y\sigma_m^z)$ and $\boldsymbol{\mu}_m^2 = (\tau_m^y, \tau_m^x\sigma_m^x, \tau_m^x\sigma_m^y, \tau_m^x\sigma_m^z)$. Numerically, we find from our mean-field analysis that the ground state has the properties that the vectors $\langle \boldsymbol{\mu}_m^n \rangle$, $n = 1, 2$, have the norm 1, and show 120° order, such that $\langle \boldsymbol{\mu}_{m_1}^n \rangle \cdot \langle \boldsymbol{\mu}_{m_2}^n \rangle = \cos(2\pi/3) = -\frac{1}{2}$ for neighboring sites. Thus, this specific type of 120° order is realized with 4-component vectors. More precisely, two different types of the 120° order are realized in the ground-state manifold of H_0: a right-handed and left-handed 120° order. The states of the right (left)-handed 120° order rotate in anti-clockwise (clockwise) order around the τ^z orientation along the triangular loop ($A \to B \to C$) as

$$\psi_B = e^{\mp i\tau^z \frac{2\pi}{3}} \psi_A, \quad \psi_C = e^{\mp i\tau^z \frac{4\pi}{3}} \psi_A. \tag{D4}$$

Those 120° orders are staggered such that the states in the neighboring triangles circulate in the opposite direction.

Surprisingly, the above described 120° orders have an extra degree of freedom. This degree of freedom can be revealed by analyzing the valley-projected magnetization vectors, $\langle \boldsymbol{\sigma} P^{\pm} \rangle$, which are length $1/2$ in the ground-state manifold. In one of the two valley, the magnetization is always ferromagnetic, but in the other valley a non-coplanar spin configuration is possible. This non-coplanar spin configuration can be fully characterized by the opening angle $0 \leqslant \theta \leqslant \pi$ of the magnetization vectors of the three neighboring sites. While the opening angle 0 and π correspond to two distinct spin ferromagnetic states, see below, $\pi/2$ corresponds to the coplanar 120° states.

It is possible to write down analytically the spinor wavefunctions in the A, B and C sublattices within the ground-state manifold. Up to rotations using the continuous symmetries $U(1) \times SU(2) \times SU(2)$, they take the form

$$\psi_A^+ = \frac{1}{\sqrt{2}} \begin{pmatrix} 1 \\ 1 \\ 0 \\ 0 \end{pmatrix},\ \psi_B^+ = \frac{1}{\sqrt{2}} \begin{pmatrix} 1 \\ -\frac{1}{2} + i\frac{\sqrt{3}}{2}\cos\theta \\ 0 \\ i\frac{\sqrt{3}}{2}\sin\theta \end{pmatrix},$$
$$\psi_C^+ = \frac{1}{\sqrt{2}} \begin{pmatrix} 1 \\ -\frac{1}{2} - i\frac{\sqrt{3}}{2}\cos\theta \\ 0 \\ -i\frac{\sqrt{3}}{2}\sin\theta \end{pmatrix} \tag{D5}$$

if the spins in the + valley order ferromagnetically. If the spins in the − valley order ferromagnetically, one finds instead (again up to transformations by the continuous symmetries $U(1) \times SU(2) \times SU(2)$)

$$\psi_A^- = \frac{1}{\sqrt{2}} \begin{pmatrix} 1 \\ 1 \\ 0 \\ 0 \end{pmatrix},\ \psi_B^- = \frac{1}{\sqrt{2}} \begin{pmatrix} -\frac{1}{2} - i\frac{\sqrt{3}}{2}\cos\theta \\ 1 \\ -i\frac{\sqrt{3}}{2}\sin\theta \\ 0 \end{pmatrix},$$
$$\psi_C^- = \frac{1}{\sqrt{2}} \begin{pmatrix} -\frac{1}{2} + i\frac{\sqrt{3}}{2}\cos\theta \\ 1 \\ i\frac{\sqrt{3}}{2}\sin\theta \\ 0 \end{pmatrix}. \tag{D6}$$

In both cases, θ is the opening angle characterizing the chiral spin order. An opening angle $\theta \neq 0, \pi, \pi/2$ leads to a finite valley-projected chirality $\chi^{\pm} = \langle \boldsymbol{\sigma} P^{\pm} \rangle_A \cdot (\langle \boldsymbol{\sigma} P^{\pm} \rangle_B \times \langle \boldsymbol{\sigma} P^{\pm} \rangle_C)$. Using the Ψ^+ solutions above, we obtain

$$\chi^+ = 0, \qquad \chi^- = \frac{3}{16}\sqrt{3}\cos\theta\sin^2\theta, \tag{D7}$$

while for the Ψ^- solution we find

$$\chi^+ = -\frac{3}{16}\sqrt{3}\cos\theta\sin^2\theta, \qquad \chi^- = 0. \tag{D8}$$

Ground states have an arbitrary θ, and thus an arbitrary $-\frac{1}{8} \leqslant \chi^- \leqslant \frac{1}{8}$ for the ψ^+ states or $-\frac{1}{8} \leqslant \chi^+ \leqslant \frac{1}{8}$

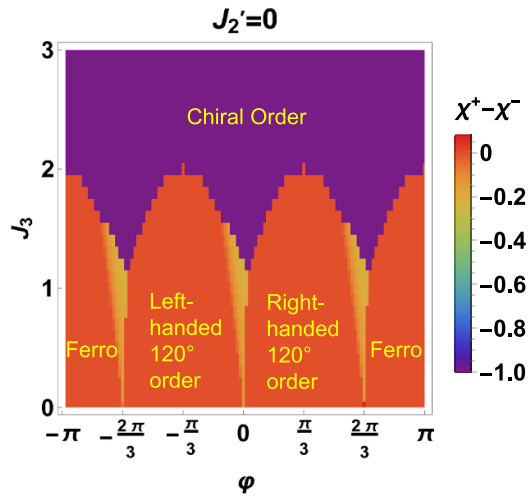

Figure 10. Mean-field phase diagram with the order parameter $(\chi^+ - \chi^-)$ in (φ, J_3) parameter space. $J_2' = 0$ and $J_2 = 1$. This diagram extends figure 3(a), which only covers small φ (defined modulo $2\pi/3$) and weak J_3 near the highly singular points. While three different types of coplanar phase (two 120° orders and a ferromagnetic order) are realized in weak J_3, the chiral order achieves the maximal values of chirality $\chi^+ - \chi^- = -1$ for sufficiently strong $J_3 > 0$ (purple region).

for the ψ^- states. For $\theta = 0$ or $\theta = \pi$, the ψ^+ and ψ^- solutions coincide (up to trivial phases). The states with $\theta = 0$ or π in equation (D5) are spin-ferromagnet in both of the valleys, but have the distinct 120° order with the left or right handedness, respectively.

Expanding H_0, at a energy minimum, in terms of three 4-component complex states, $|\psi_m^0\rangle \to |\psi_m^0\rangle + |\delta\psi_m\rangle$ with $m = A, B, C$, up to the second order, we obtain seven zero-modes among $3 \times (8-2) = 18$ degrees of freedom. Those seven zero-modes show explicitly that the ground-state manifold is 7-dimensional. Six of this seven modes arise from the spontaneously broken continuous symmetries, the 7th mode, in contrast, is related to a change of θ, thus links states which are not related by symmetry. An exception of this counting argument are the ferromagnetic states at $\theta = 0$ or $\theta = \pi$, which have a higher symmetry. They have nine zero modes, from which five arise from spontaneously broken symmetries while two each describe changes of the opening angle θ either in the valley $+$ or the $-$ sector. Note that there are two such modes per sector as magnetization vectors can tilt in two different directions starting from the ferromagnetic configuration.

In the main text, we discuss the mean-field phase diagram arising from small perturbations around the $\varphi = 0$ point, see figure 3. In figure 10 we show the analog of figure 3(a) but for an extended parameter range where φ varies from $-\pi$ to π and we also allow for large values of J_3. We find three types of non-chiral phases (red) which show either ferromagnetic or a 120° order in the vectors $\langle \boldsymbol{\mu}_n \rangle$ with $n = 1, 2$.

Importantly, the phase diagram shows singular points not only at $\varphi = 0$ but also at $\varphi = \pm\frac{2\pi}{3}$. Those singular points can be understood by the enhanced symmetry of the $\varphi = 0$ state discussed above and the transformation of equation (D2) which can be used to map the states at $\varphi = \pm\frac{2\pi}{3}$ to $\varphi = 0$. Due to the τ^z rotation, equation (D2), as adding φ by $2\pi/3$ successively, the phase changes from a left-handed 120° ordered phase → a right-handed 120° phase → a ferromagnetic phase (more precisely, in the vectors $\langle \boldsymbol{\mu}_n \rangle$ with $n = 1, 2$), and back to the left-handed 120° phase again. Such a transition between different types of 120° order was recently studied in the moiré Hubbard model [66].

Since the $\varphi = 0$ and $\varphi = \pm 2\pi/3$ points with $J_3 = J_2' = 0$ have a large, degenerate ground-state manifold, even small perturbations which lift this degeneracy can lead to a giant effect close to all three points as shown in figure 10. Note that the state with finite chiral order in either the $+$ or $-$ sector, also breaks the discrete valley symmetry leading to a finite $\langle \tau^z \rangle \neq 0$. For sufficiently large J_3 (cf figure 10), the τ^z symmetry is maximally broken with $|\langle \tau^z \rangle| = 1$ and also the chirality takes its maximal value, $\chi^+ - \chi^- = -1$ (purple region).

Appendix E. Spin-wave theory

In this appendix, we perform a spin wave calculation in $J_2' = J_3 = 0$ and $\varphi = 2\pi n/3$, $n \in \mathbb{Z}$, where ground states are highly degenerate. The motivation of this spin wave calculation is to investigate the effect of thermal and quantum fluctuation in such a highly degenerate ground-state manifold. We show that by the thermal order-by-disorder mechanism, the system selects spin ferromagnetic states in both of the valley sectors from the ground-state manifold. This is contrasted with that the quantum order-by-disorder mechanism favors 120° spin order in one valley and ferromagnetic order in the other valley. The thermal order-by-disorder mechanism leads to a mass gap linear in temperature for the soft modes related with the opening angle θ. Expanding around the classical ground states (i.e. spin-ferromagnet in both of the valleys), we show that a finite chirality $\chi^\pm$ is induced at finite temperatures by the θ-related soft modes. The non-analytic temperature dependence of the chirality arises from the linear mass gap of the soft modes in temperatures. These results remarkably match with results of the classical Monte-Carlo simulation.

We first start by developing a spin wave theory for $SU(4)$ operators. Spin wave theories become exact in certain large M limits, where M parametrize representations of the group. In the $SU(2)$ case one uses the size of the spin s (with $M = 2s$) and performs a $1/s$ expansion. In the $SU(4)$ case, we choose a totally symmetric representation of the $SU(4)$ operators by (i) writing the operators with *bosonic* creation and annihilation operators, $a_i^\dagger, a_i$ ($i = 1, \ldots, 4$ and we suppress

an extra site index here), and (ii) fix the number of bosons (per site) to be M using

$$\hat{\Gamma}^{\ell} = \sum_{i,i'=1,\ldots,4} \hat{a}_i^{\dagger} \gamma^{\ell}_{ii'} \hat{a}_{i'}, \qquad M = \sum_{i=1}^{4} \hat{a}_i^{\dagger} \hat{a}_i. \quad \text{(E1)}$$

Furthermore, we add an extra factor $1/M$ in front of the Hamiltonian, $H \to H/M$, to make the large M limit well defined, see below. The $M = 1$ case corresponds to the fundamental representation of $SU(4)$, realized if a single electron is localized on each site. While we are interested in this limit, the large M theory to useful to derive a spin-wave theory in a controlled way.

Within the functional integral formalism, the partition function of our system is expressed as

$$\mathcal{Z} = \int D[\bar{a}, a] D\lambda e^{-\int \mathrm{d}\tau \left(\sum_{i,s,\boldsymbol{n}} \bar{a}_{i,s,\boldsymbol{n}} \partial_\tau a_{i,s,\boldsymbol{n}} + \frac{1}{M} H(\bar{a},a) + i \sum_{s,\boldsymbol{n}} \lambda_{s,\boldsymbol{n}} (M - \sum_{i=1}^{4} \bar{a}_{i,s,\boldsymbol{n}} a_{i,s,\boldsymbol{n}}) \right)}, \quad \text{(E2)}$$

where $a_{i,s,\boldsymbol{n}}$ are *complex* fields and the Lagrange multipliers $\lambda_{s,\boldsymbol{n}}$ are used to implement the constraint on each site. Rescaling the boson fields as $a_{i,s,\boldsymbol{n}} = \sqrt{M} \tilde{a}_{i,s,\boldsymbol{n}}$ and using that H is quartic in these operators, we arrive

$$\mathcal{Z} = \int D[\bar{\tilde{a}}, \tilde{a}] D\lambda e^{-M S_{\mathrm{eff}}}, \quad S_{\mathrm{eff}} = \int_0^{\beta} \mathrm{d}\tau \left(\sum_{i,s,\boldsymbol{n}} \bar{\tilde{a}}_{i,s,\boldsymbol{n}} \partial_\tau \tilde{a}_{i,s,\boldsymbol{n}} + H(\bar{\tilde{a}}, \tilde{a}) - i \sum_{s,\boldsymbol{n}} \lambda_{s,\boldsymbol{n}} \left(\sum_{i=1}^{4} \bar{\tilde{a}}_{i,s,\boldsymbol{n}} \tilde{a}_{i,s,\boldsymbol{n}} - 1 \right) \right). \quad \text{(E3)}$$

Due to the factor M in front of S_{eff}, the functional integral in the large M limit is dominated by its saddle point and fluctuations around the saddle point, which are controlled by $1/M$. Saddle point solutions can be obtained by solving $\frac{\partial S_{\mathrm{eff}}}{\partial \tilde{a}_{i,s,\boldsymbol{n}}}|_{\tilde{a}_{\mathrm{sp}}, \lambda_{\mathrm{sp}}} = \frac{\partial S_{\mathrm{eff}}}{\partial \bar{\tilde{a}}_{i,s,\boldsymbol{n}}}|_{\tilde{a}_{\mathrm{sp}}, \lambda_{\mathrm{sp}}} = \frac{\partial S_{\mathrm{eff}}}{\partial \lambda_{s,\boldsymbol{n}}}|_{\tilde{a}_{\mathrm{sp}}, \lambda_{\mathrm{sp}}} = 0$. Static saddle point solutions exactly correspond to the zero-temperature mean-field solutions with $\lambda_{s,\boldsymbol{n}} = \lambda_{\mathrm{sp}}$ being the mean-field energy per site. Expanding S_{eff} up to second order around the saddle point solutions, the resulting action captures physics of spin wave excitations. Although this saddle point approximation becomes more accurate with large M, it also provides a good approximation even to the $M = 1$ case. Hereafter M is set to 1, unless otherwise stated.

To understand the effect of quantum or thermal fluctuation on the degenerate ground-state manifold of H_0 (equation (D3)), we use the approach explained above for $J_2' = J_3 = 0$ and $\varphi = 2\pi n/3$, $n \in \mathbb{Z}$ where the mean-field solution is highly degenerate. As a reference state around which the action (equation (E3)) is expanded, we take the spinor wavefunctions $\psi_s^0(\alpha = \pm, \theta) = \psi_s^{\alpha}(\theta)$ (equations (D5) and (D6)) that depend on the opening angle θ and α. α represents the valley sector in which the spin has the ferromagnetic order. Then, low-energy states associated with the spin wave excitation can be generally written, up to normalization, as

$$\psi_s(\alpha, \theta) \sim \psi_s^0(\alpha, \theta) + \frac{1}{\sqrt{M}} \sum_{i=1}^{3} \hat{a}_{s,i} \delta\psi_{s,i}(\alpha, \theta). \quad \text{(E4)}$$

Here $\delta\psi_{s,i}$ are three 4-component unit vectors perpendicular to the reference state $\psi_s^0(\pm, \theta)$. At this point, we find it useful to switch back from the functional integral formalism to the operator formalism, where it is more easy to keep track of commutation relation. Expanding to the second order in $\hat{a}_{s,i}$ and performing the Fourier transform to momentum space, the Hamiltonian has a Bogoliubov-de Gennes (BdG) form

$$H_{\mathrm{BdG}} = \frac{1}{2} \sum_{\boldsymbol{k}} \begin{pmatrix} \hat{a}_{\boldsymbol{k}}^{\dagger} & \hat{a}_{-\boldsymbol{k}} \end{pmatrix} \begin{pmatrix} A(\boldsymbol{k}) & B(\boldsymbol{k}) \\ B^*(-\boldsymbol{k}) & A^*(-\boldsymbol{k}) \end{pmatrix} \begin{pmatrix} \hat{a}_{\boldsymbol{k}} \\ \hat{a}_{-\boldsymbol{k}}^{\dagger} \end{pmatrix} - \frac{1}{2} \sum_{\boldsymbol{k}} \mathrm{Tr} A(\boldsymbol{k}). \quad \text{(E5)}$$

Here $A(\boldsymbol{k})$ and $B(\boldsymbol{k})$ are 9×9 matrices in the basis of sublattice $s = A, B, C$ and $i = 1, 2, 3$ representing three directions perpendicular to $\psi_s^0(\alpha, \theta)$, and fulfill the condition $A(\boldsymbol{k}) = A^{\dagger}(\boldsymbol{k})$ and $B(\boldsymbol{k}) = B^T(-\boldsymbol{k})$, respectively. The diagonalization of the bosonic BdG Hamiltonian, equation (E5), should be taken with special care. To fulfill the bosonic commutation relation for the eigenmodes, the transformation matrix $T(\boldsymbol{k})$ for the diagonalization has to satisfy the paraunitarity condition $T^{\dagger}(\boldsymbol{k}) \Sigma^z T(\boldsymbol{k}) =$

$T(\boldsymbol{k})\Sigma^z T^\dagger(\boldsymbol{k}) = \Sigma^z$ with the third Pauli matrix Σ^z acting on the Nambu space. As a consequence, $T(\boldsymbol{k})$ and the corresponding eigen energies are obtained from diagonalizing the matrix $\Sigma^z H(\boldsymbol{k})$ instead [67]. Using this diagonalization scheme, one obtains

$$\begin{aligned} H_{\mathrm{BdG}} &= \frac{1}{2}\sum_{\boldsymbol{k}} \begin{pmatrix} \hat{\gamma}_{\boldsymbol{k}}^\dagger & \hat{\gamma}_{-\boldsymbol{k}} \end{pmatrix} \begin{pmatrix} E(\boldsymbol{k}) & 0 \\ 0 & E(-\boldsymbol{k}) \end{pmatrix} \begin{pmatrix} \hat{\gamma}_{\boldsymbol{k}} \\ \hat{\gamma}_{-\boldsymbol{k}}^\dagger \end{pmatrix} \\ &\quad - \frac{1}{2}\sum_{\boldsymbol{k}} \mathrm{Tr} A(\boldsymbol{k}) \\ &= \sum_{\boldsymbol{k}}\sum_{n=1}^{9} E_{\boldsymbol{k},n}(\alpha,\theta)\left(\hat{\gamma}_{\boldsymbol{k},n}^\dagger \hat{\gamma}_{\boldsymbol{k},n} + \frac{1}{2}\right) \\ &\quad - \frac{1}{2}\sum_{\boldsymbol{k}} \mathrm{Tr} A(\boldsymbol{k}). \end{aligned} \tag{E6}$$

Here $E(\boldsymbol{k})$ is a diagonal matrix with positive elements $E_{\boldsymbol{k},n} > 0$. In the ground state the occupation of the finite-energy states vanishes and therefore the ground-state energy is given by

$$E_0 \approx E_{\mathrm{MF}} + \frac{1}{2}\sum_{\boldsymbol{k},n} E_{\boldsymbol{k},n}(\alpha,\theta) - \frac{1}{2}\sum_{\boldsymbol{k}} \mathrm{Tr} A(\boldsymbol{k}) \tag{E7}$$

where E_{MF} is the mean-field energy. It turns out that $\mathrm{Tr} A(\boldsymbol{k})$ is independent on the expansion point (α,θ). E_0 also includes corrections arising from quantum fluctuations, computed to leading order in $1/M$. Similarly, the free energy at low temperatures can be approximated by

$$\begin{aligned} F &\approx E_{\mathrm{MF}} + \frac{1}{2}\sum_{\boldsymbol{k},n} E_{\boldsymbol{k},n}(\alpha,\theta) - \frac{1}{2}\sum_{\boldsymbol{k}} \mathrm{Tr} A(\boldsymbol{k}) \\ &\quad + \frac{1}{\beta}\sum_{\boldsymbol{k},n} \log(1 - e^{-\beta E_{\boldsymbol{k},n}(\alpha,\theta)}). \end{aligned} \tag{E8}$$

The spectrum of excitation $E_{\boldsymbol{k},n}(\alpha,\theta)$ depends on the chosen mean-field state $\psi_s^0(\alpha,\theta)$ even in cases where the mean-field energy is exactly the same. This is shown in figure 11 where the excitation spectrum is shown for an expansion around (i) a state with ferromagnetic spin-order ($\theta = 0$), (ii) a state with chiral spin chirality ($\theta = \pi/4$) and (iii) a coplanar spin-state ($\theta = \pi/2$). The excitation spectrum differs in the number of Goldstone modes and also in its high-energy spectrum. Thus both E_0 and F will depend on the chosen ground state within the mean-field ground-state manifold. Nature will select the state with the lowest (free-) energy. This is an example of the 'order by disorder' mechanism, where quantum or thermal fluctuations select one specific ordered state out of a larger manifold.

To be able to compare with the result of classical Monte Carlo calculations, it is useful to evaluate the free energy (E8) in the classical limit, $E_{\boldsymbol{k},n} \ll T$, where we obtain

$$F^{\mathrm{cl}} \approx E_{\mathrm{MF}} + T\sum_{\boldsymbol{k},n} \log(\beta E_{\boldsymbol{k},n}(\alpha,\theta)). \tag{E9}$$

Figures 12(a) and (b) shows the free energy with different ground states, characterized by the opening angle θ. As shown in figure 12(a), the free energy at zero temperature has a minimum at the state with the opening angle $\theta = \pi/2$, i.e. the spin-coplanar 120° order in one valley (keeping the ferromagnetic order in the other valley). The selection of the states are achieved by the quantum order-by-disorder mechanism. In contrast, the thermal fluctuations select distinct states from the quantum fluctuations as shown from the classical free energy in figure 12(b). The thermal order-by-disorder mechanism leads to a selection of the spin ferromagnetic order in both of the valley sectors ($\theta = 0$ or π). Thus, our system is one of the rare cases where quantum and classical fluctuations select very different types of ground states. Technically this arises, because the classical fluctuations select the state where the *geometric* average (sum of logarithms) of the energies $E_{\boldsymbol{k},n}$ is lowest, while quantum fluctuations select the state with the lowest *arithmetic* average.

In figure 12(c), we show the free energy, equation (E8), as function of temperature for the states with $\theta = \pi/2$ and $\theta = 0, \pi$. Formally, the calculation predicts a first order transition from the spin-coplanar state to the spin-ferromagnetic state upon increasing T. The transition temperature, $T \approx 3.8 J_2$, is, however, so high that the expansion around the $T = 0$ mean-field, which underlies equation (E8), is not expected to be valid any more. Our classical Monte-Carlo simulations (see main text) show that there is no long-ranged order at this temperature.

The discussion of the free energy given above explains that the classical Monte Carlo calculations reported in the main text obtain a spin-ferromagnetic ground state ($\theta = 0, \pi$) in the limit $T \to 0$. For the classical model, the spin-wave theory should become exact for low T, as it captures Gaussian fluctuations around the classical ground state. We can therefore use it to explain two numerical results shown in figures 4(b) and (c). The spin-chirality, $\chi^+ - \chi^-$, obtains a finite expectation value at $T > 0$, which rises in a singular way as function of temperature. Furthermore, the ferromagnetic order parameter obtains a correction linear in T with a prefactor which increases for increasing system size. Remarkably, such a system-size dependence is largely absent for the spin-chirality and only visible at the lowest temperatures, see inset of figure 4(b).

The suppression of the order parameter is a well-known consequence of the Mermin–Wagner theorem: the thermal occupation of the Goldstone modes gives rise to a correction of order $-T\log 1/N$ to the order parameter, where N is the linear system size. This effect is clearly visible in the numerics. In an infinite system, $N \to \infty$, long-range order is expected

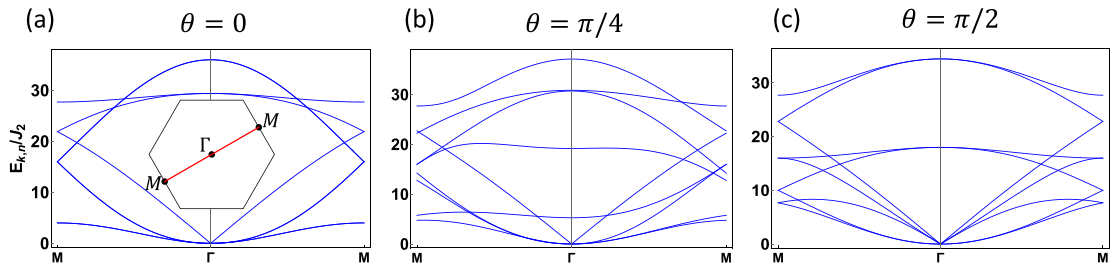

Figure 11. Spin-valley excitation spectra for an expansion around (a) a state with ferromagnetic spin order ($\theta = 0$), (b) a state with chiral spin chirality ($\theta = \pi/4$) and (c) a coplanar spin-state ($\theta = \pi/2$). The spectra are drawn along the red line ($M - \Gamma - M$) in the Brillouin zone shown in the inset of panel (a). The excitation spectra differ in the number of Goldstone modes. Panel (a): four quadratic modes, (more precisely, for each valley, a Goldstone mode corresponding to the ferromagnetic order and a θ-related soft mode) and a linear mode, Panel (b): three quadratic modes and a linear mode, Panel (c): two quadratic and three linear modes.

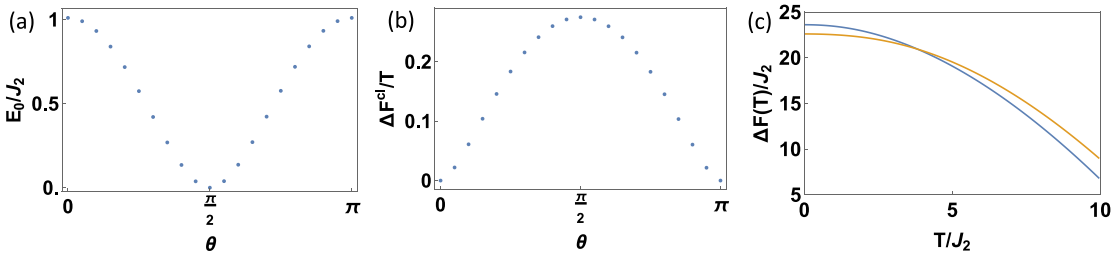

Figure 12. Order-by-disorder mechanisms. (a) The ground-state energy per site (equation (E7)) as function of θ, parameterizing the opening angle of valley-projected spins on the three sublattices. By the quantum order-by-disorder mechanism, the state with the opening angle $\theta = \pi/2$ (i.e. the spin-coplanar 120° order) is selected from the ground-state manifold. (b) In the classical model, the free energy $F^{\rm cl}$, equation (E9), obtains at low T a correction linear in T from thermal fluctuations. In contrast with the quantum order-by-disorder mechanism, the thermal order-by-disorder leads to the selection of the spin ferromagnetic order in both of the valley sectors ($\theta = 0$ or π). (c) Free energy as function of temperature. As the thermal order-by-disorder mechanism selects the distinct ground states from the quantum order-by-disorder mechanism, a first-order phase transition occurs at an intermediate temperature, $k_{\rm B}T \sim 3.8 J_2$.

to be absent at any finite T with a correlation length which is exponentially large in $1/T$.

More surprising is the finite chirality and its unusual temperature dependence. It is straightforward to expand the valley-projected chirality operators

$$\chi^{\pm} = \langle \boldsymbol{\sigma}_{m_1} P^{\pm}_{m_1} \cdot (\boldsymbol{\sigma}_{m_2} P^{\pm}_{m_2} \times \boldsymbol{\sigma}_{m_3} P^{\pm}_{m_3}) \rangle \approx \chi^{\pm}_{\rm cl} + \frac{1}{V} \sum_{\boldsymbol{k},n} \chi^{\pm}_{\boldsymbol{k},n} (\langle \hat{\gamma}^{\dagger}_{\boldsymbol{k},n} \hat{\gamma}_{\boldsymbol{k},n} \rangle + 1/2) \quad \text{(E10)}$$

where $V = N^2$ is the number of sites in the system, $\chi^{\pm}_{\rm cl}$ is the chirality of the mean-field ground state and $\chi^{\pm}_{\boldsymbol{k},n}$ is a numerically determined weight factor which encodes how much chirality an excitation with quantum numbers n and $\boldsymbol{k}$ carries.

To compare to our classical Monte Carlo simulation, we use this formula expanding around the spin-ferromagnetic state, $\theta = 0, \pi$, where $\chi^{\pm}_{\rm cl} = 0$. In the classical limit, $T \gg E_{\boldsymbol{k},n}$, we have to replace $\langle \hat{\gamma}^{\dagger}_{\boldsymbol{k},n} \hat{\gamma}_{\boldsymbol{k},n} \rangle + \frac{1}{2}$ by $T/E_{\boldsymbol{k},n}$ and we obtain

$$\langle \hat{\chi}^{\pm} \rangle = \frac{1}{V} \sum_{\boldsymbol{k},n} \chi^{\pm}_{\boldsymbol{k},n} \frac{T}{E_{\boldsymbol{k},n}(\alpha,\theta)}. \quad \text{(E11)}$$

Importantly, $\chi^{\pm}_{\boldsymbol{k},n}$ turns out to be finite for $\boldsymbol{k} \to 0$ for one of the modes, which we label by $n_{\pm}$, with $E_{\boldsymbol{k},n_{\pm}} \approx c_\theta k^2$ for $\boldsymbol{k} \to 0$. Numerically, we obtain $\chi^{\pm}_{0,n_{\pm}} = \mp 2.60$ (when expanding around $\theta = 0$, signs are opposite when expanding around $\theta = \pi$) and $c_\theta \approx 3.1$. The $n_{\pm}$ modes describe fluctuations of θ which naturally give rise to a finite spin chirality (note that $\chi^{\pm} \approx \mp \frac{3\sqrt{3}}{16} \theta^2$ according to equations (D7) and (D8)).

Thus, equation (E14) predicts for the $\theta = 0$ state a nominally *divergent* contribution to the chirality of the form

$$\langle \hat{\chi}^{\pm} \rangle \approx \frac{1}{V} \sum_{\boldsymbol{k}} \chi^{\pm}_{0,n_{\pm}} \frac{T}{J_2 c_\theta k^2} \approx \mp 0.11 \frac{T}{J_2} \ln \left[\frac{k_0}{k_{\rm min}} \right], \quad \text{(E12)}$$

where k_0 denotes a UV cutoff to the k sum and we introduced ad hoc an minimal momentum $k_{\rm min}$ as an infrared cutoff. In three dimensions, the analog calculation would give $T(c_1 - c_2 k_{\rm min})$.

Thus the question arises, what sets the value of the infrared cutoff $k_{\rm min}$. Importantly, it is *not* set by the system size but by the fact that the θ-modes $n_{\pm}$ are *not* true Goldstone modes. While within mean-field changes of θ in the two valley-sectors do not cost

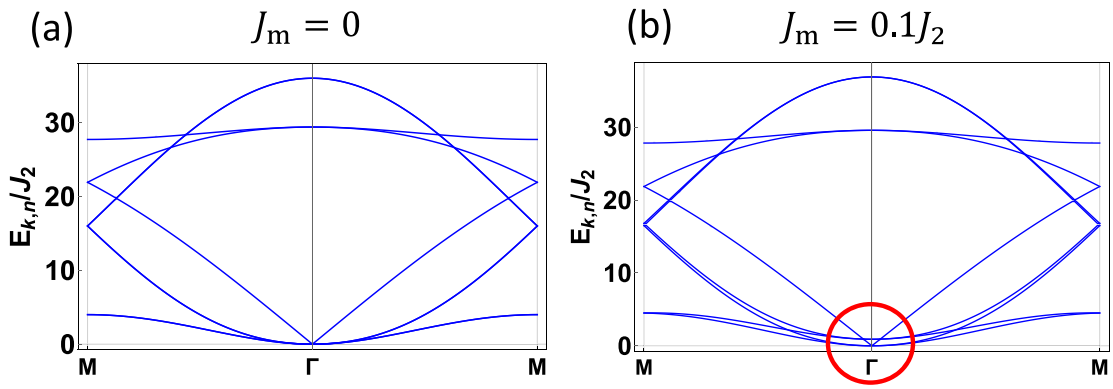

Figure 13. Mass gap of θ-modes, $n_\pm$ modes (see the text), induced by the Hamiltonian equation (E15) to stabilize the ferromagnetic spin order. The excitation spectra are obtained from an expansion of a ferromagnetic state ($\theta = 0$), which is an energy minimum of the mean-field theory. The two $n^\pm$ modes from two valleys acquire the mass gap as shown in near Γ point (the red circle).

any energy. This is, however, not the correct result. As shown in figure 12(b), the free energy near the classical minima ($\theta_0 = 0, \pi$) is approximately described by

$$F^{\rm cl}_{\alpha,\theta} \approx F^{\rm cl}_{\alpha,\theta_0} + \frac{1}{2} c_1 T(\theta - \theta_0)^2. \qquad \text{(E13)}$$

This term induces a finite mass $\sim T$ to the $n_\pm$ modes resulting in an effective IR cutoff $k_{\rm min} \sim \sqrt{T}$,

$$\langle \hat{\chi}^+ - \hat{\chi}^- \rangle \approx \pm 0.22 \frac{T}{J_2} \ln\left[\sqrt{T_0/T}\right], \qquad \text{(E14)}$$

where the sign depends on whether we expand around $\theta = 0$ or $\theta = \pi$ and T_0 is some UV cutoff energy. Equation (E14) explains the singular temperature dependence observed in the Monte Carlo numerics, figure 4 and also the approximate absence of finite-size effects in this quantity as long as $k_{\rm min} N \gtrsim 1$. In three dimensions, the analog calculation would give a correction of the form $c_1 T - c_2 T^{3/2}$.

To see how the mass gap enters the dispersion of the $n_\pm$ modes, we add a Hamiltonian, given by

$$H_{\rm mass} = J_{\rm m} \sum_{\langle m,m' \rangle} ((\boldsymbol{\sigma} P^+)_m \cdot (\boldsymbol{\sigma} P^+)_{m'} + (\boldsymbol{\sigma} P^-)_m \cdot (\boldsymbol{\sigma} P^-)_{m'}). \qquad \text{(E15)}$$

Note that this Hamiltonian stabilizes the spin-ferromagnetic state ($\theta = 0, \pi$), but opens up a mass gap in the $n^\pm$ modes. Expanding around the $\theta = 0$ state, one of the classical minima with $H_0 + H_{\rm mass}$, we obtain the excitation spectra shown in figure 13. Each of the $n_\pm$ modes acquires a mass gap with dispersion $E_{\boldsymbol{k},n_\pm} \sim \boldsymbol{k}^2 + J_{\rm m}^2$. Therefore, the mass gap nicely provides an effective infrared cutoff $k_{\rm min} \sim J_{\rm m}$, as discussed above.

The discussion given above applies to the classical model. In the quantum case, when we expand around a ferromagnetic solution (stabilized, e.g. by $J_2' < 0$), $|\langle \hat{\chi}^+ - \hat{\chi}^- \rangle|$ is finite even for $T = 0$. In the spin-planar phase, $\theta = \pi/2$ (stabilized by quantum fluctuations in the pure J_2 model and also obtained for $J_2' > 0$), in contrast, $\chi^\pm$ vanishes by symmetry, see below.

Two symmetries are most important for the discussion of the spin chirality. First, a 180° rotation of both spin and space around, e.g. the $\hat{y}$ axis maps $\chi^\pm$ to $-\chi^\pm$. Second, the inversion symmetry maps $\chi^\pm$ to $-\chi^\mp$.

The spin-ferromagnetic state (with a 120° valley order) breaks 180° rotation symmetry but is inversion symmetric. Thus $\chi^+ + \chi^- = 0$ while $\chi^+ - \chi^-$ is finite. The state with coplanar 120° spin-order (realized in the quantum J_2 model), in contrast, has both symmetries and thus $\chi^\pm = 0$. This is also reflected in figure 5 of the main text which shows that $|\chi^+ - \chi^-|$ is only finite in the spin-ferromagnetic phase.

Appendix F. Semi-classical Monte Carlo

In this appendix, we provide a more detailed description of the our semi-classical Monte Carlo implementation. We note that a very similar description (by some of us) for a filling of two instead of one electron per site can be found in [68]. We then conclude this manuscript by presenting additional numerical data elucidating the type of phase transitions separating the disordered and the two ordered states found in the $J_2 - J_2'$ model (see figure 5).

F.1. Implementation

To calculate finite-temperature observables, we perform semi-classical Monte Carlo calculations using the Metropolis algorithm [58] with local updates. Instead of a classical spin configuration, however, we need to update the product-state wavefunction $|\Psi\rangle = \prod_m |\Psi_m\rangle$, where $|\Psi_m\rangle$ is a single-site, 4-component,

normalized wave function. To this end, we parameterize the single-site wave-function as

$$|\psi_m\rangle = \sum_{j=1}^{4} b_m^j |\gamma^j\rangle\,, \tag{F1}$$

with normalized, 4-dimensional, complex-valued vectors $|\mathbf{b_m}| = 1$. The states $|\gamma^j\rangle$ constitute a basis of the local Hilbert space, for which we simply choose

$$|\gamma^j\rangle \in \{|\uparrow +\rangle, |\downarrow +\rangle, |\uparrow -\rangle, |\downarrow -\rangle\} \tag{F2}$$

where $\sigma = (\uparrow, \downarrow)$ is the spin and $\alpha = (+, -)$ the valley quantum number, labeling the eigenvalues of σ^z and τ^z, respectively. Subtracting the normalization and a local arbitrary phase, a state can therefore be parametrized by $N^2 \cdot (8-2)$ real numbers. In the Monte Carlo calculation, however, it turns out beneficial to simply include the redundancy of the phase, which does not affect any of our observables, and work with all components of $\mathbf{b}_m$. To perform a local Metropolis update, we consequently need to be able to uniformly sample the space of normalized, complex valued, 4-dimensional vectors. Such vectors can be understood to live on a 7-dimensional hypersphere (7-sphere), parameterized by the real- and imaginary part of each component. To uniformly sample on a 7-sphere, one can simply draw $7+1$ normally distributed numbers and then normalize the resulting vector [69]. Sampling on the full sphere, however, leads to very low acceptance rates for low temperatures, which in turn results in a slow convergence of the results. Instead, we adapt [70] and utilize the *Gaussian trial move*, which generates a new local state in the 'vicinity' of the original as

$$\mathbf{b}'_m = \frac{\mathbf{b}_m + \sigma_g \mathbf{\Gamma}}{|\mathbf{b}_m + \sigma_g \mathbf{\Gamma}|}, \tag{F3}$$

where $\mathbf{\Gamma}$ is a 4-dimensional complex vector, with the real and imaginary part of each component sampled from a normal distribution. The value of σ_g controls the 'step-size' of the update. Staring with a large $\sigma_g = 60$ and then adjusting σ_g every ten Monte Carlo sweeps according to

$$\sigma_g \to \frac{0.5}{1-R}\sigma_g, \tag{F4}$$

where R is the acceptance rate during the last ten sweeps, this very quickly tunes the overall acceptance rate to approximately 50% leading to significant speedup in convergence at lower temperatures.

We begin each Monte Carlo run with a thermalization phase, typically lasting for $N_t = 1 \times 10^6$ sweeps, in which the temperature is continuously lowered from a large initial value of $T_1 = 3|J_2|$ to the desired temperature T. More precisely, for the first $3/4N_t$ sweeps the temperature is lowered by a multiplication with the factor $(T/T_1)^{\frac{4}{3N_t}}$ after each sweep. For the remaining $\frac{1}{4}N_t$ sweeps the temperature is kept constant. During the thermalization phase σ_g is adjusted using the procedure described above. After thermalization, we start the measurement phase, typically for $N_m = 10 \times 10^6$ sweeps, where we keep T and σ_g constant and perform measurements every tenth sweep. The statistical evaluation of the measurements is done using the `BinningAnalysis` Julia Package [71].

F.2. Phase transitions

The finite-temperature phase diagram of the $J_2 - J_2'$ model shown in figure 5 features three distinct phases: A disordered phase at high temperature, a state with 120° order in $\boldsymbol{\mu}^{1,2}$ and ferromagnetic order in $\boldsymbol{\sigma}$, and a similar state where the spin instead shows 120° order in one valley. Figure 14 shows Monte Carlo data for all three of the corresponding phase transitions separating the different phases.

The transition from the disordered state into the state with ferromagnetic spin order ($J_2'/J_2 < 0.1$) features a seemingly continuous energy as a function of temperature and the energy distribution at the transitions shows only one Gaussian peak, indicating a continuous phase transition, a thermal crossover or a weak first-order transition. As discussed in the main text and shown in figure 10, the sharp rise of the chirality $|\langle\chi^+ - \chi^-\rangle|$, accompanied by the breaking of a discrete $\mathbb{Z}_2$ symmetry, is mostly independent from N, strongly suggesting a phase transition instead of a crossover. Very close to T_c, however, $|\langle\chi^+ - \chi^-\rangle|$ strongly fluctuates between different Monte Carlo runs, even when repeating runs at fixed T, leading to large statistical errors which prohibit us from determining the precise nature of the phase transition.

In contrast, the transition separating the two ordered states ($0 < J_2'/J_2 < 0.1$), as well as the transition between the disordered phase and the phase with spin 120° order ($J_2'/J_2 > 0.1$) show a discontinuity in the energy and a bimodal energy distribution at the critical temperature, both becoming more pronounced for larger lattice sizes N. This suggests that both phase transitions are of first-order. To measure the strength of the first-order transitions, we obtain the associated latent heat by fitting double Gaussians to the energy distribution at the critical temperature and calculating the distance between the two peaks. The resulting latent heat for both first-order transitions is shown in figure 15, which exhibit a sizable latent heat of up to $\Delta\epsilon/J_2 \approx 0.07$ and $\Delta\epsilon/J_2 \approx 0.08$, respectively, indicating strong first-order transitions. When approaching the transition into the ferromagnetic spin order, where the thermal phase transition appears continuous, the latent heat smoothly vanishes.

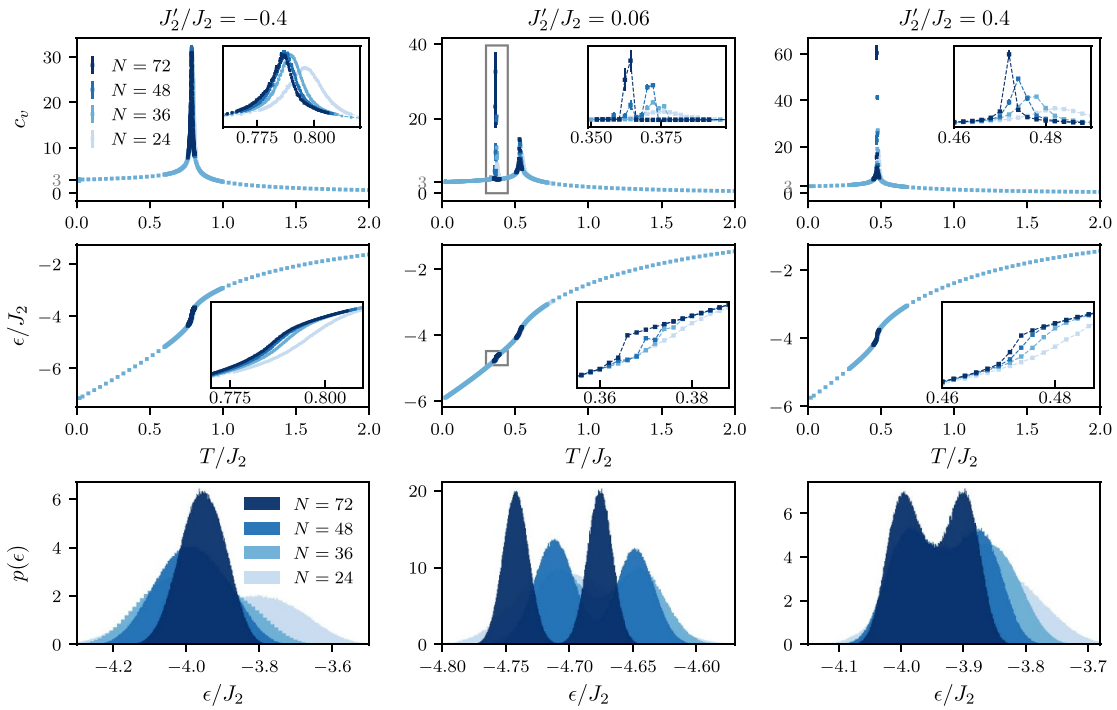

Figure 14. Thermal phase transitions in the $\mathbf{J}_2 - \mathbf{J}_2'$ model. Monte Carlo data showing the specific heat c_v, energy per site ε and energy distribution $p(\epsilon)$ in the three principal phase transitions we observe, obtained for linear system sizes $N = 24, 36, 48, 72$. At $J_2'/J_2 = -0.4$ (left column) a transition from the disordered state to the ordered state with 120° order in $\mu^{1,2}$ and ferromagnetic order in $\boldsymbol{\sigma} P^{\pm}$ occurs. The continuous decrease in energy and the single peak structure of the energy distribution at the transition temperature suggest a continuous or a weak first-order phase transition. At $J_2'/J_2 = 0.06$ (middle column) the peak in c_v at higher temperature corresponds to the same transition as for $J_2'/J_2 = -0.4$. The second peak, which is shown in the insets, corresponds to the transition between the two ordered states, where the spin changes from ferromagnetic to 120° order in one valley. The kink in the energy and the bimodal structure of the energy distribution, which become more pronounced with increasing N, imply a first-order transition. For $J_2'/J_2 = 0.4$ (right column) the system directly transitions from the disordered state into the ordered state with 120° spin order, also showing signatures of a first-order transition.

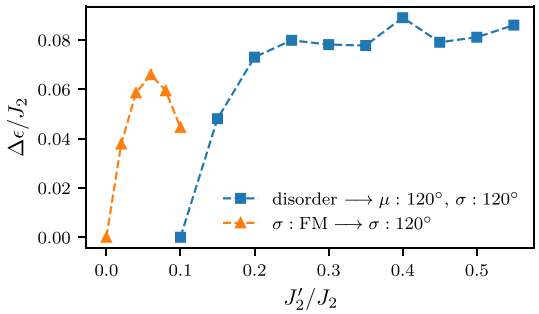

Figure 15. Latent heat of the first-order phase transitions. The latent heat $\boldsymbol{\Delta\epsilon}$ is obtained from the Monte Carlo data at lattice size $N = 72$ by fitting double Gaussians to the energy distribution at the critical scale and calculating the distance between the two peaks. For $0 < J_2'/J_2 < 0.1$ a first-order phase transition between the two ordered states of figure 5 occurs, at which in one valley the spin transitions from ferromagnetic to coplanar 120° order. At $J_2' > 0.1J_2$ the disordered state directly transitions into the state with 120° spin order. Both transitions show a sizable latent heat, indicating a strong first-order transition.

ORCID iDs

Jeyong Park https://orcid.org/0009-0002-3029-6503
Lasse Gresista https://orcid.org/0000-0003-0185-7391
Simon Trebst https://orcid.org/0000-0002-1479-9736
Achim Rosch https://orcid.org/0000-0002-6586-5721
Jinhong Park https://orcid.org/0000-0003-3570-6356

References

[1] Geim A K and Grigorieva I V 2013 Van der Waals heterostructures *Nature* **499** 419
[2] Andrei E Y, Efetov D K, Jarillo-Herrero P, MacDonald A H, Mak K F, Senthil T, Tutuc E, Yazdani A and Young A F 2021 The marvels of moiré materials *Nat. Rev. Mater.* **6** 201

[3] Chen G *et al* 2019 Signatures of tunable superconductivity in a trilayer graphene moiré superlattice *Nature* **572** 215
[4] Xie Y-M, Zhang C-P, Hu J-X, Mak K F and Law K T 2022 Valley-polarized quantum anomalous hall state in moiré $MoTe_2/WSe_2$ heterobilayers *Phys. Rev. Lett.* **128** 026402
[5] Jin C *et al* 2021 Stripe phases in WSe2/WS2 moiré superlattices *Nat. Mater.* **20** 940
[6] Xu Y, Liu S, Rhodes D A, Watanabe K, Taniguchi T, Hone J, Elser V, Mak K F and Shan J 2020 Correlated insulating states at fractional fillings of moiré superlattices *Nature* **587** 214
[7] Li T *et al* 2021 Quantum anomalous Hall effect from intertwined moiré bands *Nature* **600** 641
[8] Cao Y *et al* 2018a Correlated insulator behaviour at half-filling in magic-angle graphene superlattices *Nature* **556** 80
[9] Cao Y, Fatemi V, Fang S, Watanabe K, Taniguchi T, Kaxiras E and Jarillo-Herrero P 2018b Unconventional superconductivity in magic-angle graphene superlattices *Nature* **556** 43
[10] Bistritzer R and MacDonald A H 2011 Moiré bands in twisted double-layer graphene *Proc. Natl Acad. Sci. USA* **108** 12233
[11] Tarnopolsky G, Kruchkov A J and Vishwanath A 2019 Origin of magic angles in twisted bilayer graphene *Phys. Rev. Lett.* **122** 106405
[12] Po H C, Zou L, Vishwanath A and Senthil T 2018 Origin of Mott insulating behavior and superconductivity in twisted bilayer graphene *Phys. Rev.* X **8** 031089
[13] Kennes D M, Lischner J and Karrasch C 2018 Strong correlations and $d + id$ superconductivity in twisted bilayer graphene *Phys. Rev.* B **98** 241407
[14] Wu F, MacDonald A H and Martin I 2018 Theory of phonon-mediated superconductivity in twisted bilayer graphene *Phys. Rev. Lett.* **121** 257001
[15] Lian B, Wang Z and Bernevig B A 2019 Twisted bilayer graphene: a phonon-driven superconductor *Phys. Rev. Lett.* **122** 257002
[16] Roy B and Juričić V 2019 Unconventional superconductivity in nearly flat bands in twisted bilayer graphene *Phys. Rev.* B **99** 121407
[17] Yankowitz M, Chen S, Polshyn H, Zhang Y, Watanabe K, Taniguchi T, Graf D, Young A F and Dean C R 2019 Tuning superconductivity in twisted bilayer graphene *Science* **363** 1059
[18] Isobe H, Yuan N F and Fu L 2018 Unconventional superconductivity and density waves in twisted bilayer graphene *Phys. Rev.* X **8** 041041
[19] Choi Y *et al* 2019 Electronic correlations in twisted bilayer graphene near the magic angle *Nat. Phys.* **15** 1174
[20] Kerelsky A *et al* 2019 Maximized electron interactions at the magic angle in twisted bilayer graphene *Nature* **572** 95
[21] Xie Y *et al* 2021 Fractional Chern insulators in magic-angle twisted bilayer graphene *Nature* **600** 439
[22] Ledwith P J, Tarnopolsky G, Khalaf E and Vishwanath A 2020 Fractional Chern insulator states in twisted bilayer graphene: an analytical approach *Phys. Rev. Res.* **2** 023237
[23] Song Z-D and Bernevig B A 2022 Magic-angle twisted bilayer graphene as a topological heavy fermion problem *Phys. Rev. Lett.* **129** 047601
[24] Thomson A, Chatterjee S, Sachdev S and Scheurer M S 2018 Triangular antiferromagnetism on the honeycomb lattice of twisted bilayer graphene *Phys. Rev.* B **98** 075109
[25] Bultinck N, Khalaf E, Liu S, Chatterjee S, Vishwanath A and Zaletel M P 2020 Ground state and hidden symmetry of magic-angle graphene at even integer filling *Phys. Rev.* X **10** 031034
[26] Kwan Y H, Wagner G, Soejima T, Zaletel M P, Simon S H, Parameswaran S A and Bultinck N 2021 Kekulé spiral order at all nonzero integer fillings in twisted bilayer graphene *Phys. Rev.* X **11** 041063
[27] Hofmann J S, Khalaf E, Vishwanath A, Berg E and Lee J Y 2022 Fermionic Monte Carlo study of a realistic model of twisted bilayer graphene *Phys. Rev.* X **12** 011061
[28] Chou Y-Z and Sarma S D 2022 Kondo lattice model in magic-angle twisted bilayer graphene (arXiv:2211.15682)
[29] Mora C, Regnault N and Bernevig B A 2019 Flatbands and perfect metal in trilayer moiré graphene *Phys. Rev. Lett.* **123** 026402
[30] Khalaf E, Kruchkov A J, Tarnopolsky G and Vishwanath A 2019 Magic angle hierarchy in twisted graphene multilayers *Phys. Rev.* B **100** 085109
[31] Park J M, Cao Y, Watanabe K, Taniguchi T and Jarillo-Herrero P 2020 Tunable Phase Boundaries and Ultra-Strong Coupling Superconductivity in Mirror Symmetric Magic-Angle Trilayer Graphene (arXiv:2012.01434)
[32] Chen S *et al* 2021 Electrically tunable correlated and topological states in twisted monolayer–bilayer graphene *Nat. Phys.* **17** 374
[33] He M, Li Y, Cai J, Liu Y, Watanabe K, Taniguchi T, Xu X and Yankowitz M 2020 Symmetry breaking in twisted double bilayer graphene *Nat. Phys.* **17** 26
[34] Ramires A and Lado J L 2021 Emulating heavy fermions in twisted trilayer graphene *Phys. Rev. Lett.* **127** 26401
[35] Park J M, Cao Y, Xia L-Q, Sun S, Watanabe K, Taniguchi T and Jarillo-Herrero P 2022 Robust superconductivity in magic-angle multilayer graphene family *Nat. Mater.* **21** 877
[36] San-Jose P and Prada E 2013 Helical networks in twisted bilayer graphene under interlayer bias *Phys. Rev.* B **88** 121408
[37] Efimkin D K and MacDonald A H 2018 Helical network model for twisted bilayer graphene *Phys. Rev.* B **98** 35404
[38] Ramires A and Lado J L 2018 Electrically tunable gauge fields in tiny-angle twisted bilayer graphene *Phys. Rev. Lett.* **121** 146801
[39] Rickhaus P *et al* 2018 Transport through a network of topological channels in twisted bilayer graphene *Nano Lett.* **18** 6725
[40] Huang S, Kim K, Efimkin D K, Lovorn T, Taniguchi T, Watanabe K, MacDonald A H, Tutuc E and LeRoy B J 2018 Topologically protected helical states in minimally twisted bilayer graphene *Phys. Rev. Lett.* **121** 37702
[41] Yoo H *et al* 2019 Atomic and electronic reconstruction at the van der Waals interface in twisted bilayer graphene *Nat. Mater.* **18** 448
[42] Xu S G *et al* 2019 Giant oscillations in a triangular network of one-dimensional states in marginally twisted graphene *Nat. Commun.* **10** 4008
[43] Chou Y-Z, Wu F and Das Sarma S 2020 Hofstadter butterfly and Floquet topological insulators in minimally twisted bilayer graphene *Phys. Rev. Res.* **2** 033271
[44] De Beule C, Dominguez F and Recher P 2020 Aharonov-Bohm oscillations in minimally twisted bilayer graphene *Phys. Rev. Lett.* **125** 096402
[45] De Beule C, Dominguez F and Recher P 2021 Network model and four-terminal transport in minimally twisted bilayer graphene *Phys. Rev.* B **104** 195410
[46] Chou Y-Z, Wu F and Sau J D 2021 Charge density wave and finite-temperature transport in minimally twisted bilayer graphene *Phys. Rev.* B **104** 045146
[47] Attig J, Park J, Scherer M M, Trebst S, Altland A and Rosch A 2021 Universal principles of moiré band structures *2D Mater.* **8** 044007
[48] Xu S *et al* 2021 Tunable van Hove singularities and correlated states in twisted monolayer–bilayer graphene *Nat. Phys.* **17** 619
[49] Kugel' K I and Khomskii D I 1982 The Jahn-Teller effect and magnetism: transition metal compounds *Sov. Phys. Usp.* **25** 231
[50] Wietek A and Läuchli A M 2017 Chiral spin liquid and quantum criticality in extended $S = 1/2$ Heisenberg models on the triangular lattice *Phys. Rev.* B **95** 035141
[51] Gong S S, Zhu W, Zhu J X, Sheng D N and Yang K 2017 Global phase diagram and quantum spin liquids in a spin-1/2 triangular antiferromagnet *Phys. Rev.* B **96** 075116

[52] Szasz A, Motruk J, Zaletel M P and Moore J E 2020 Chiral spin liquid phase of the triangular lattice Hubbard model: a density matrix renormalization group study *Phys. Rev.* X **10** 021042
[53] Chen B B, Chen Z, Gong S S, Sheng D N, Li W and Weichselbaum A 2022 Quantum spin liquid with emergent chiral order in the triangular-lattice Hubbard model *Phys. Rev.* B **106** 094420
[54] Sur S, Udupa A and Sen D 2022 Driven Hubbard model on a triangular lattice: tunable Heisenberg antiferromagnet with a chiral three-spin term *Phys. Rev.* B **105** 054423
[55] Kuhlenkamp C, Kadow W, Imamoglu A and Knap M 2022 Tunable topological order of pseudo spins in semiconductor heterostructures (arXiv:2209.05506)
[56] Stoudenmire E M, Trebst S and Balents L 2009 Quadrupolar correlations and spin freezing in $S = 1$ triangular lattice antiferromagnets *Phys. Rev.* B **79** 214436
[57] Hickey C and Paramekanti A 2014 Thermal phase transitions of strongly correlated bosons with spin-orbit coupling *Phys. Rev. Lett.* **113** 265302
[58] Landau D P and Binder K 2014 *A Guide to Monte Carlo Simulations in Statistical Physics* (Cambridge: Cambridge University Press)
[59] Mermin N D and Wagner H 1966 Absence of ferromagnetism or antiferromagnetism in one- or two-dimensional isotropic Heisenberg models *Phys. Rev. Lett.* **17** 1133
[60] Villain J, Bidaux R, Carton J-P and Conte R 1980 Order as an effect of disorder *J. Phys.* **41** 1263
[61] Chalker J T, Holdsworth P C W and Shender E F 1992 Hidden order in a frustrated system: properties of the Heisenberg Kagomé antiferromagnet *Phys. Rev. Lett.* **68** 855
[62] Lian Y, Rosch A and Goerbig M O 2016 SU(4) skyrmions in the $\nu = \pm 1$ quantum hall state of graphene *Phys. Rev. Lett.* **117** 056806
[63] Feng W, Hanke J-P, Zhou X, Guo G-Y, Blügel S, Mokrousov Y and Yao Y 2020 Topological magneto-optical effects and their quantization in noncoplanar antiferromagnets *Nat. Commun.* **11** 118
[64] Wittig P, Dominguez F, Beule C D and Recher P 2023 Localized states coupled to a network of chiral modes in minimally twisted bilayer graphene (arXiv:2303.03901 [cond-mat.mes-hall])
[65] Jung J and MacDonald A H 2014 Accurate tight-binding models for the π bands of bilayer graphene *Phys. Rev.* B **89** 035405
[66] Wietek A, Wang J, Zang J, Cano J, Georges A and Millis A 2022 Tunable stripe order and weak superconductivity in the Moiré Hubbard model *Phys. Rev. Res.* **4** 043048
[67] Colpa J 1978 Diagonalization of the quadratic boson Hamiltonian *Physica* A **93** 327
[68] Gresista L, Kiese D, Trebst S and Scherer M M 2023 Spin-valley magnetism on the triangular moiré lattice with SU(4) breaking interactions (arXiv:2303.01244)
[69] Muller M E 1959 A note on a method for generating points uniformly on *n*-dimensional spheres *Commun. ACM* **2** 19–20
[70] Alzate-Cardona J D, Sabogal-Suárez D, Evans R F L and Restrepo-Parra E 2019 Optimal phase space sampling for Monte Carlo simulations of Heisenberg spin systems *J. Phys.: Condens. Matter* **31** 095802
[71] Bauer C and Freyer F 2020 BinningAnalysis.jl: standard error estimation tools (Zenodo) (available at: https://doi.org/10.5281/zenodo.3603347)